



**HAL**  
open science

# Tunable multidispersive bands of inductive origin in piezoelectric phononic plates

K. Mekrache, R. Sainidou, P. Rembert, N. Stefanou, Bruno Morvan

## ► To cite this version:

K. Mekrache, R. Sainidou, P. Rembert, N. Stefanou, Bruno Morvan. Tunable multidispersive bands of inductive origin in piezoelectric phononic plates. *Journal of Applied Physics*, 2021, 130 (19), pp.195106. 10.1063/5.0065184 . hal-03479298

**HAL Id: hal-03479298**

**<https://normandie-univ.hal.science/hal-03479298>**

Submitted on 14 Dec 2021

**HAL** is a multi-disciplinary open access archive for the deposit and dissemination of scientific research documents, whether they are published or not. The documents may come from teaching and research institutions in France or abroad, or from public or private research centers.

L'archive ouverte pluridisciplinaire **HAL**, est destinée au dépôt et à la diffusion de documents scientifiques de niveau recherche, publiés ou non, émanant des établissements d'enseignement et de recherche français ou étrangers, des laboratoires publics ou privés.

Copyright

# Tunable multidispersive bands of inductive origin in piezoelectric phononic plates

K. Mekrache,<sup>1</sup> R. Sainidou,<sup>1</sup> P. Rembert,<sup>1, a)</sup> N. Stefanou,<sup>2</sup> and B. Morvan<sup>1</sup><sup>1)</sup>Laboratoire Ondes et Milieux Complexes UMR CNRS 6294, UNIHAVRE, Normandie University, 75 rue Bellot, 76600 Le Havre, France<sup>2)</sup>Section of Condensed Matter Physics, National and Kapodistrian University of Athens, Panepistimioupolis, GR-157 84 Athens, Greece

(Dated: 18 October 2021)

A variety of multidispersive, localized or extended in frequency, bands, induced by inductance-based external electric circuits in piezoelectric phononic plates, is studied both theoretically and experimentally in this work. Their origin, tightly related to an equivalent  $LC$ -circuit behavior is analyzed in detail and their interaction with the Lamb-like guided modes of the plate is also discussed. These bands, easily tuned by the choice of the parameters of the external electric circuitry lead to a non-destructive, real-time control of the dispersion characteristics of these structures. Our device and analysis can find application in improvement of surface acoustic wave (SAW) components, by offering additional degrees of freedom.

## 1 I. INTRODUCTION

Controlling the dispersion of elastic waves has become a key issue when dealing with sound mitigation, vibration energy harvesting and, more generally, applications in which elastic waves have to be guided, collimated or trapped. The use of metamaterials has been an important step towards the feasibility of this control<sup>1-3</sup> by shaping the dispersion relation of these complex media. Several approaches have been proposed, the most common being the periodic structuration of the medium (phononic crystal) leading to folding of its frequency bands and opening up of band gaps. To tailor the band structure at subwavelength regime, a very promising means has been the use of the locally-resonant materials that produce strong dispersive effects related to negative effective bulk modulus and mass density<sup>4-6</sup>. These structures suffer, however, from an intrinsic narrow frequency range behavior of the resonant phenomena. To overcome this limitation, a more sophisticated structuring has been recently proposed, facilitated by the use of new manufacturing techniques, such as 3D printing. The concepts of rainbow metamaterials, gradient index and hierarchical metamaterials allowing to model the dispersion of the waves on a broader frequency range have emerged<sup>7-9</sup>.

However all these attractive properties of metamaterials, even in the case of wide-range frequency phenomena, will stay less appealing, especially for application purposes, if the question of frequency tunability in their response is not answered. For a fixed geometrical arrangement of the constituents of the complex medium, the resulting frequency response cannot be adapted in real time in a real device. A simple way to introduce this frequency tunability/agility lies in the use of active components whose control can be achieved with the help

of an externally applied field (magnetic<sup>10,11</sup>, electric<sup>12</sup>, thermal<sup>13,14</sup>, and radiative<sup>15,16</sup>). The mechanical properties (mass density, elastic moduli) of the active component are thus modified, leading to reversible changes in its frequency band structure. Among others, piezoelectric-based structures have been shown to be excellent candidates for the real-time control of the propagation of elastic waves. The electro-mechanical coupling, naturally present in these materials, offers a versatile tool to shape the effective elastic properties of the metamaterial, through a variety of electrically controlled external conditions applied at the structure<sup>17-26</sup>.

In this paper, we use a piezoelectric material as a substrate (plate) on which metallic strips (electrodes) are structured. In previous works<sup>23-26</sup>, some of us have shown that propagation of Lamb-like guided modes in these phononic crystal piezoceramic plates exhibits an interesting tunable character easily controlled by external electric circuits through appropriate electric boundary conditions (EBCs) applied at the metallic strips. In particular, the band structure of the plate is significantly modulated by the presence of electric resonant modes originating from the external inductance-loads coupled to the effective capacitive behavior of the piezoelectric plate. Some basic methodological tools of our analysis are already presented in Ref. 26. Here, we extend them in order to give a synthetic panel that these systems can offer. We review under a new light some of the possibilities to mould the dispersion characteristics of tunable localized bands originating from an equivalent  $LC$ -circuit behavior, inherent in piezoelectric phononic plates, when loaded with inductance external circuits. We focus on three typical representative cases including external  $L$ -based loads that generate, each of them, a variety of multidispersive, tunable bands of electromagnetic (EM) origin, easily controlled via the external circuitry parameters (the inductance, in our case). These cases, first given in a qualitative schematic manner, cover, respectively, low, intermediate and higher frequency regions in a typical dispersion plot. Moreover, compared to previ-

<sup>a)</sup>Electronic mail: [pascal.rembert@univ-lehavre.fr](mailto:pascal.rembert@univ-lehavre.fr)

This is the author's peer reviewed, accepted manuscript. However, the online version of record will be different from this version once it has been copyedited and typeset.  
PLEASE CITE THIS ARTICLE AS DOI: 10.1063/5.0065184

ous works<sup>23–26</sup>, an important improvement of our exper-  
imental device—especially its electronic part—is made,  
towards a wider range of choices in real-time control and  
automatization, combined to a robust and promising sig-  
nal processing technique leading to a finer analysis of the  
experimental data. Usually, surface acoustic wave (SAW)  
devices offer only input and output ports, restricting the  
analysis exclusively in the frequency domain. Our de-  
vice, allows to probe the surface waves along their path,  
thus offering the wavevector projection along this path  
as an additional degrees of freedom, which could provide  
an improvement in the domain of SAW components.

The paper is organized as follows. In Sec. II we present  
the general characteristics of the materials and structures  
considered in this study, and provide all necessary details  
concerning the experimental setup employed for our mea-  
surements, as well as the methods and techniques used in  
the analysis of the experimental data and in the numer-  
ical calculations, that follow in Sec. III. For the different  
structures under study, the analysis of their dispersion  
properties, strongly influenced by the external loads, in  
terms of underlying physical mechanisms responsible for  
these effects, as well as in comparison with their experi-  
mental observation, constitute the main part of Sec. III,  
before concluding the paper in Sec. IV.

## II. MATERIALS AND METHODS

### A. Sample structure

We shall be concerned, in this study, with thin homo-  
geneous piezoceramic plates whose both surfaces are de-  
corated with periodic one-dimensional (1D) arrays (lattice  
constant  $a_0$ ) of parallel and face-to-face metallic strips of  
width  $w$  and negligible thickness. A schematic represen-  
tation of the structure is given in Fig. 1(a). The plate  
is made of PZT (Navy VI) and in all theoretical calcu-  
lations presented in this paper it will be considered to  
be infinite along  $x_1$ - and  $x_2$ -directions that coincide with  
the transversely isotropic plane of the piezoceramic ma-  
terial; the  $x_3$ -axis coincides with the polarization axis of  
the material.

The sample used in the experiments, is a finite square-  
shaped plate (edge length 48 mm and thickness  $h =$   
1.6 mm), as can be seen in Fig. 1(b), on both sides of  
which silver strips (rectangular electrodes) have been de-  
posited periodically; their thickness is of the order of  
15  $\mu\text{m}$  and will be neglected in what follows. In the  
real structure, the lattice period dictated by the metallic  
strips (width  $w = 0.7$  mm, separation gap  $s = 0.3$  mm)  
equals  $a_0 = s + w = 1$  mm, but as we have already ex-  
plained in previous works<sup>24–26</sup> the true lattice constant  
of the crystal  $a$  can be non-destructively extended to be a  
multiple of  $a_0$ , controlled through the application of ap-

propriate EBCs at each pair of (up- and down-side) elec-  
trodes. The latter is connected in the most general case  
to external electric circuits of characteristic impedance  
 $Z^u$  and  $Z^d$ , as schematically depicted in Fig. 1(c). In this  
manner, the elementary blocks of length  $a_0 = w + s$  may  
have identical ( $a = a_0$ ) or different ( $a = \kappa a_0$ ,  $\kappa = 2, 3, \dots$ )  
EBCs throughout the structure, thus tuning at will the  
real periodicity of the crystal. The 1D Brillouin zone  
(BZ) of the crystal is accordingly shortened; we will de-  
note its center ( $k_1 a / \pi = 0$ ) by  $\Gamma$  and its edge ( $k_1 a / \pi = 1$ )  
by  $X$ .

### B. Experimental setup

Our experimental setup, though simple, is designed in  
such a general manner to facilitate modification at will of  
the EBCs applied at each electrode by connecting exter-  
nal circuits (resistive, capacitive, and/or inductive). The  
current version has substantially improved, as compared  
to the one used in Ref. 26. First, the plate is inserted into  
a 1 mm-pitch PCI Express<sup>®</sup> edge card reader (stack-  
able female connector with 98 contacts), allowing con-  
nection of the electrodes of the crystal to different elec-  
tric impedances, through controlled switches (FST3125).  
All connections are now realized in a secure and robust  
manner avoiding any noise and parasitic effects arising  
from soldering. Second, a microcontroller (Teensy 3.6)  
is used to actuate these switches, thus making possible a  
real-time control. Apart from the first pair of electrodes  
reserved for the excitation of the plate, the remaining 47  
pairs of electrodes will be used to load the plate with ex-  
ternal circuits, as shown in Fig. 2(a). Only this part of  
the plate (we will refer to it as loaded crystal hereafter)  
will be utilized to image the frequency response of the  
structure, except otherwise stated.

A 200V-amplitude and 0.1 $\mu\text{s}$ -width pulse signal is ap-  
plied to the first pair of electrodes at the one edge of the  
piezoelectric plate, using a Panametrics 5058PR pulse  
generator, to excite guided waves within the plate. The  
incident beam penetrates into the loaded crystal and is  
reflected back at the other edge. To visualize the fre-  
quency response of the crystal, we employ an all-electric  
experimental technique (more details can be found in  
Ref. 26). After excitation of the piezoelectric plate, any  
deformations producing not negligible thickness varia-  
tions of the plate will be manifested as electric potential  
variations on the electrodes through the electromechani-  
cal coupling that takes place within the piezoelectric ma-  
terial; we exclusively measure these electric potentials  
along the plate. To this end, a second PCI card reader,  
identical to the first one used for the loading by exter-  
nal circuits, is connected to the remaining free edge of  
the plate [Fig. 2(b)]. The electric potential is recorded  
with a 10-bit quantification, at each electrode position,  
on the upper or lower side of the plate, with the help of a  
digital oscilloscope (LeCroy HRO66ZI WaveRunner), the  
ground of the pulse generator being taken as reference;

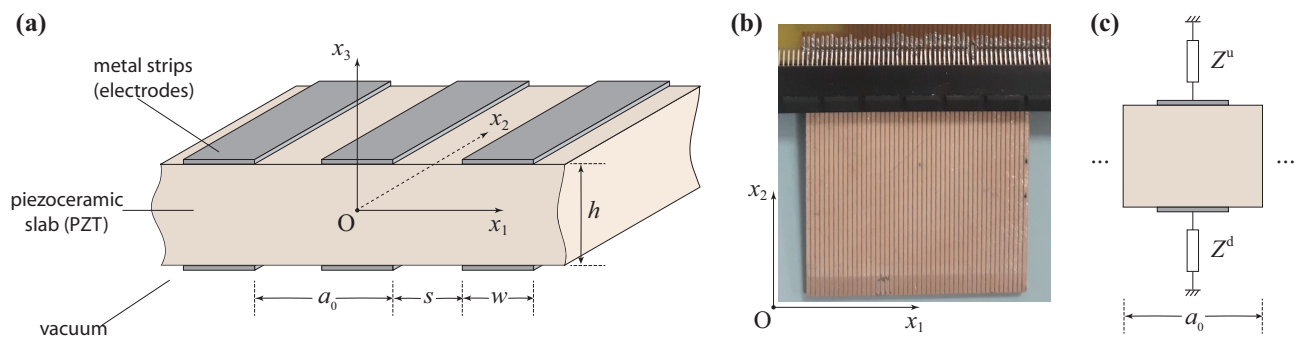


FIG. 1. (a) Schematic representation of the one-dimensional piezoelectric crystal, extended to infinity along  $x_1$ - and  $x_2$ -directions coinciding with the transversely isotropic plane of the piezoceramic material, poled across its thickness along the  $x_3$  symmetry axis. (b) An image of the fabricated sample with finite dimensions ( $48 \text{ mm} \times 48 \text{ mm} \times 1.6 \text{ mm}$ ), used in the experiments; the metallic strips (width  $w = 0.7 \text{ mm}$  and separation gap  $s = 0.3 \text{ mm}$ ) aligned along  $x_2$ -direction are connected at the top edge of the plate to a PCI reader. The structure consists of  $N = 48$  elementary blocks of length  $a_0 = 1 \text{ mm}$ . In (c) an elementary block of the structure loaded with electric circuits of impedance  $Z^u$  (upper plate side) and  $Z^d$  (lower plate side).

TABLE I. Material parameters for PZT (Navy VI), used in the calculations.

Material Property	Symbol	Value <sup>a</sup>
Elastic coefficients $c_{pq}^E$ [GPa]	$c_{11}^E$	114.0
	$c_{12}^E$	75.7
	$c_{13}^E$	70.0 (72.4)
	$c_{33}^E$	107.0 (111.0)
	$c_{44}^E$	20.0 (26.3)
	$c_{66}^E$ <sup>b</sup>	19.2
	Piezoelectric coefficients $e_{ip}$ [ $\text{C m}^{-2}$ ]	$e_{15}$
	$e_{31}$	-2.92
	$e_{33}$	20.3 (23.4)
Relative permittivity coefficients $\epsilon_{pq}^S$	$\epsilon_{11}^S$	2120.
	$\epsilon_{33}^S$	1980.
Mass density [ $\text{kg m}^{-3}$ ]	$\rho$	7510. <sup>c</sup> (7780.)

<sup>a</sup> In the parenthesis, we give —if different— the initial values as provided by the manufacturer<sup>28</sup>.

<sup>b</sup>  $c_{66}^E = \frac{1}{2}(c_{11}^E - c_{12}^E)$ .

<sup>c</sup> Measured.

183 the time window chosen is typically set to  $250 \mu\text{s}$ , with a  
184 sampling period equal to  $5 \text{ ns}$ , allowing to observe a few  
185 forward and backward traveling waves after reflections  
186 at the edges of the plate. Each measured signal is then  
187 averaged 30 times to improve the signal-to-noise ratio.  
188 The above settings ensure a sufficiently high Nyquist fre-  
189 quency and accurate resolution of the spectra obtained  
190 through fast Fourier transforms (FFT).

### 191 C. Simulations and signal processing

192 All band structure calculations shown in this paper  
193 were obtained by the use of a finite-element commercial  
194 package<sup>27</sup> (except otherwise stated). Assuming trans-  
195 lational invariance along  $x_2$ -direction, the unit cell is

196 reduced to a rectangle and the metallic strips to lines  
197 of zero thickness, able to host surface electric charges.  
198 The classical constitutive equations of piezoelectricity  
199 (stresses as functions of strains and electric field) apply  
200 at the surface of the rectangle. The boundary condi-  
201 tions are: (i) continuity of all fields between adjacent  
202 cells and periodic (Bloch) conditions at the left and right  
203 boundaries of the same cell, and (ii) at the upper and  
204 lower edges of the cell, free stress conditions, together  
205 with discontinuity of the normal component of the elec-  
206 tric displacement field related to the surface charge den-  
207 sity across the interface, assuming a uniform distribu-  
208 tion of charge along the line representing the metallic strip.  
209 Under this last assumption, the whole electrode is seen  
210 as an electric node, where Ohm's relation involving ex-  
211 ternal impedance loads can be applied. We recall that  
212 a full comparison between an ab-initio analytical model  
213 using the above assumptions and this FEM approach was  
214 given in Ref. 25, leading to practically identical (graphi-  
215 cally indiscernible) results for the band diagrams of these  
216 systems. We note in passing that only the positive part of  
217 the BZ will be represented, since the dispersion diagrams  
218 are symmetric with respect to the vertical (frequency)  
219 axis, in all cases discussed here. The material param-  
220 eters (elastic, piezoelectric and coupling constants) for  
221 PZT used in the simulations are shown in Table I and  
222 were determined by adjusting the dispersion relation of  
223 a floating-potential crystal to the corresponding experi-  
224 mental data. The experimental dispersion relation  $\omega(k_1)$ ,  
225  $\omega = 2\pi f$  being the angular frequency, was obtained, af-  
226 ter applying a 2D FFT of the potential signals  $V(x_{1,n}, t)$   
227 measured at each electrode position  $x_{1,n}$ ,  $n = 2, 3, \dots, 48$ ,  
228 of the upper and lower side of the corresponding finite  
229 plate, following the procedure described in Ref. 26. The  
230 simulation results agree very well with the experimental  
231 data (tolerance better than 3.2%).

232 The floating-potential EBCs were used as a bench-  
233 mark; we are, however, interested in more complex unit  
234 cells. For the systems under study, the dispersion plot

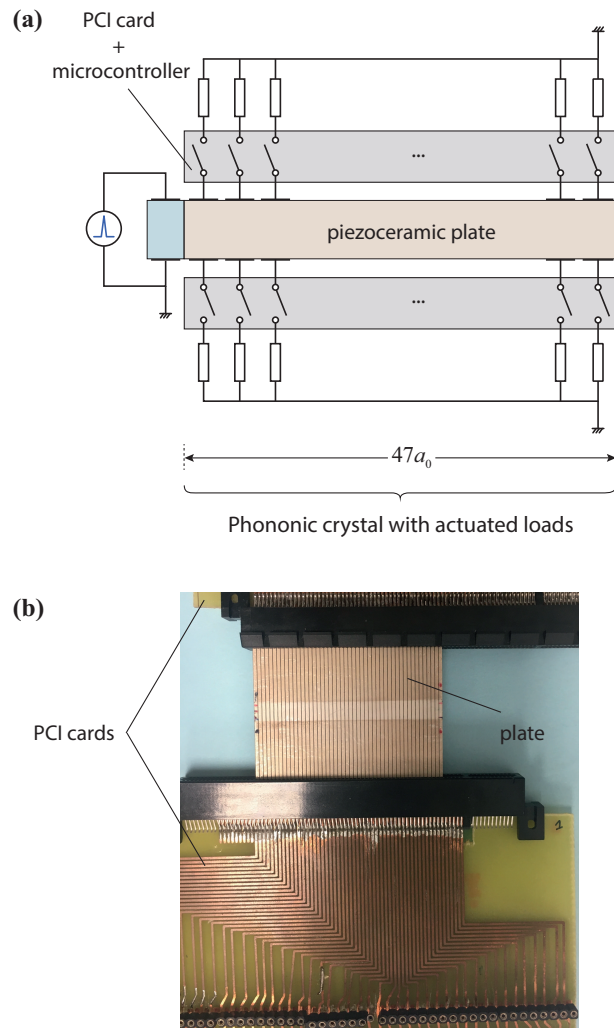


FIG. 2. The experimental setup used for the study of the phononic plate of Fig. 1: (a) schematic representation, and, (b) a view of the device. Excitation takes place at the left end of the plate and loading by external circuits at its remaining part through controlled EBCs.

235 is more crowded: several eigenmode trajectories coexist  
 236 in the  $\omega$ - $k_1$  space at neighboring points and cannot be  
 237 easily resolved, after a 2D FFT is performed. To better  
 238 resolve these separate contributions, we opt for a different  
 239 method of analysis, by adapting an autoregressive model  
 240 to two dimensions (AR2D), i.e., to both space and time  
 241 directions<sup>29</sup>. The results obtained in that manner agree  
 242 with the corresponding picture obtained by a 2D FFT,  
 243 without suffering from a wide  $\omega$ - $k_1$  peak-character.

### 244 III. RESULTS AND DISCUSSION

245  
 246 In what follows, we will focus on three configurations,  
 247 all of them using inductance loads on the unit cell of the  
 248 crystal, shown schematically in the left panel of Fig. 3;

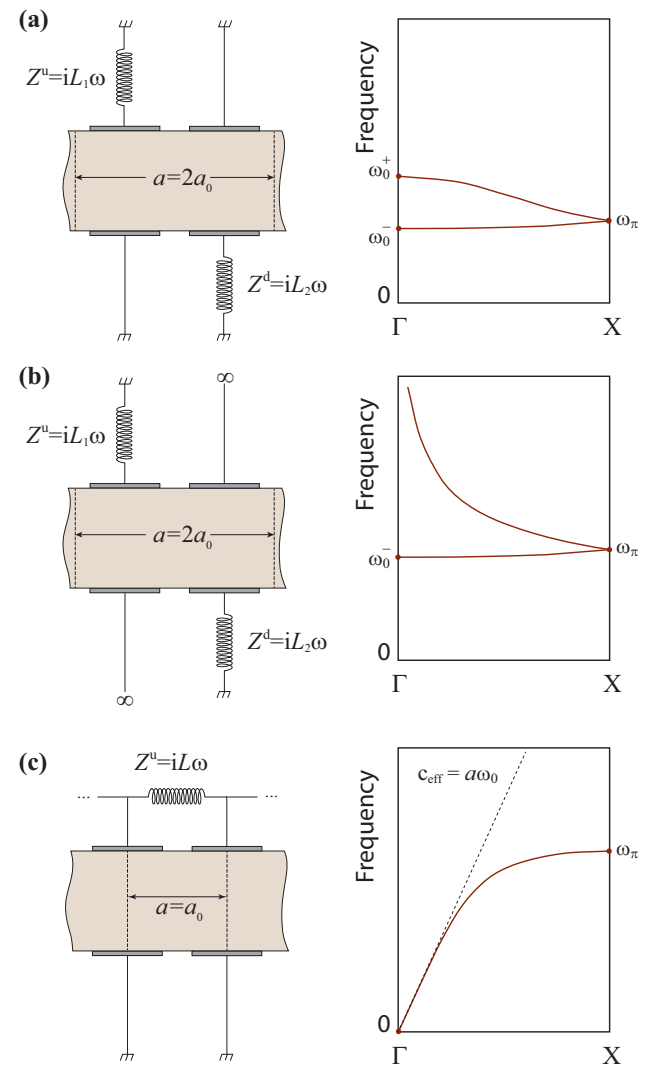


FIG. 3. The three configurations with inductive loads under study. Left panel: the unit cell of each crystal with different electric boundary conditions applied at the metallic strips [(a) grounded-inductance two-atom crystal, (b) floating-potential-inductance two-atom crystal, and (c) intercellular adjacent inductance-loaded crystal]. Right panel: schematic representation of the corresponding dispersion relation of the induced LC-origin bands (for  $L_1 = L_2$ , when applicable).

249 their interest lies on the unusual multidispersive form  
 250 of localized and/or extended frequency bands of inductive  
 251 origin that this circuitry may offer. More precisely,  
 252 the first two cases correspond to two-atom unit cells  
 253 ( $a = 2a_0$ ), constructed by combination of two antiparallel  
 254 elementary blocks (of width  $a_0$ ), each of them having  
 255 a  $L$ -load on the one side of the plate, the other-side  
 256 electrode being either shunted [Fig. 3(a)] or in floating  
 257 potential [Fig. 3(b)]. Though inspired from Ref. 26, the  
 258 resulting structures offer new possibilities, since they possess  
 259 inversion symmetry and exhibit, respectively, a set  
 260 of two flat bands of localized modes and a set of one  
 261 flat and one infinitely extended hyperbola-like frequency

bands, as schematically depicted in the right panel of Fig. 3. A third configuration [see Fig. 3(c)] consists of a  $L$ -load connecting adjacent strips, the EBCs conserve, in that case, the spatial periodicity of the metallic array ( $a = a_0$ ). The corresponding modes originating from this circuitry exhibit a linear dispersion behavior with an effective medium slope  $c_{\text{eff}} = a\omega_0$  at the long-wavelength limit which bends and tends to a zero-group-velocity branch at X point. It is worth noting that such a configuration is a direct analogue of the unit cell of a transmission line governed by the well-known telegrapher's equation.

The different characteristic angular frequencies  $\omega_0^\pm$ ,  $\omega_0$ ,  $\omega_\pi$ , appearing in Fig. 3 to describe qualitatively the dispersion of these eigenmodes at  $\Gamma$  and X points of the BZ, depend of course of the choice of  $L$  and of some characteristic capacitance values  $C$ ,  $C_s$ ,  $C_1$ , and  $C_2$  that describe effectively the intrinsic behavior of the piezoelectric plate in terms of equivalent circuits. More details are given in Appendix A. We note that this analysis for the two-atom crystals reveals higher-order interactions of capacitive origin within the plate which takes place between neighbors of adjacent cells and opposite sides, compared to previous demonstrations<sup>26</sup>.

#### A. Grounded and inductance loaded two-atom unit cell

To begin with we shall examine the case of up- and down-side inductance loads alternated with grounded strips. The unit cell is thus a two-atom molecule analog with inversion symmetry if  $L_1 = L_2$ , or with identity operation symmetry only, if  $L_1 \neq L_2$ , as shown in Fig. 3(a). Aiming to analyze its frequency band structure both theoretically and experimentally, we find it useful to focus first on the frequency response of the corresponding monoatomic crystal of lattice constant  $a = a_0$  [suppose only the left half part of the unit cell of Fig. 3(a)]. In the absence of piezoelectric coupling ( $e_{ij} = 0$ ), the eigenmodes of the crystal are separated into two independent, non-interacting subspaces: the elastic-displacement Lamb guided modes of the plate (labelled, hereafter, with A for antisymmetric and S for symmetric modes, following standard notation used for Lamb modes in plates), simply folded at the BZ edge ( $k_1 a_0/\pi = 1$ ) and the EM modes which originate from an  $LC$ -equivalent circuit behavior of the unit cell. The electric resonances of these individual  $LC$  atoms interact between each other and form a cos-like resonant band. In Fig. 4(a) we show the calculated —using a finite-element method— frequency band structure of such a crystal, the first subspace shown in gray lines, the second one in blue dotted line, extending from 1.294 MHz ( $k_1 = 0$ ) to 0.597 MHz ( $k_1 = \pi/a_0$ ). We note in passing that this zero coupling analysis, already presented in previous works<sup>24,26</sup>, can be employed to visualize the bands of EM origin before hybridization.

When two antiparallel atoms are brought together to form a two-atom unit cell as shown in Fig. 3(a) the BZ

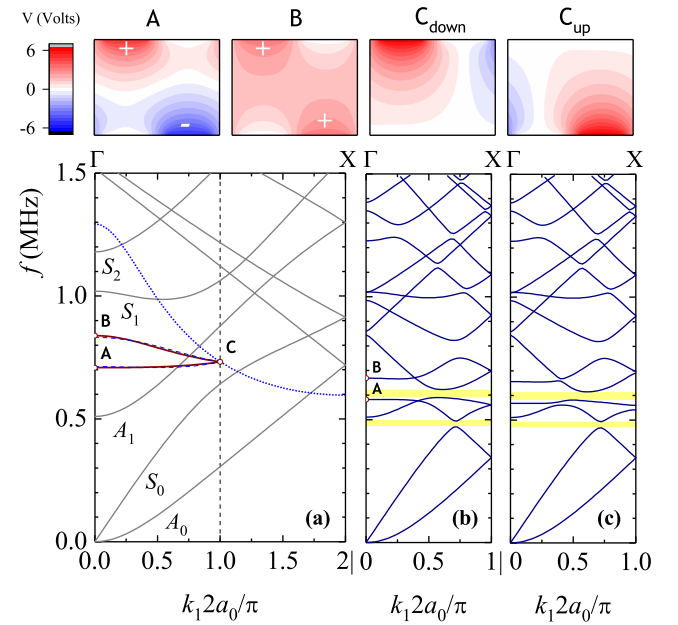


FIG. 4. (a) Calculated frequency band structure for a monoatomic crystal of lattice constant  $a = a_0$  [only the left half part of the unit cell in Fig. 3(a) with  $L_1 = 30 \mu\text{H}$  is considered] when piezoelectric coupling is switched off. The blue dotted curve spanning the whole BZ indicates the EM resonance band, while the thick red line represents the same band for the diatomic crystal of lattice constant  $a = 2a_0$  [unit cell of Fig. 3(a) with  $L_1 = L_2 = 30 \mu\text{H}$ ]; the gray lines correspond to Lamb eigenmodes of the phononic plate, labelled following standard notation. The full calculation of the band structures for the diatomic crystal of Fig. 3(a) when piezoelectric coupling is taken into account is shown in (b) for  $L_1 = L_2 = 30 \mu\text{H}$  and (c) for  $L_1 = 30 \mu\text{H}$  and  $L_2 = 33 \mu\text{H}$ . Yellow-shaded regions denote absolute frequency gaps. Top panel: Potential field plots within a unit cell for the points labelled in (a).

becomes shorter ( $a = 2a_0$ ). An additional folding at  $k_1 a_0/\pi = 0.5$  of the dispersion plot is dictated and, as a result, the EM resonant band is thus split into two separate flat minibands, a more dispersive,  $\omega^+(k_1)$ , extending from 0.839 MHz ( $k_1 = 0$ ) to 0.732 MHz ( $k_1 = \pi/a$ ), and a less dispersive,  $\omega^-(k_1)$ , extending from 0.708 MHz ( $k_1 = 0$ ) to 0.732 MHz ( $k_1 = \pi/a$ ). These bands compare very well (relative error better than  $\pm 0.9\%$ ) to a tight-binding description<sup>30</sup> with first-neighbour interactions between atomic sites [blue dashed lines in Fig. 4(a)] that leads to  $\omega^\pm(k_1) = [\omega_{\text{at}}^2 + 2\gamma_1 \cos k_1 a \pm 2\gamma_2 \cos(k_1 a/2)]^{1/2}$ ,  $\gamma_1 = \gamma(a)$ ,  $\gamma_2 = \gamma(R)$  being the overlap integrals  $\gamma$  depending on the distance  $a = 2a_0$  and  $R = \sqrt{a_0^2 + h^2} = 1.89a_0$  between the centers of the atomic potential functions and  $\omega_{\text{at}}$  the eigenfrequency of an isolated atom. By a best fitting procedure we find  $\omega_{\text{at}}/(2\pi) = 0.753$  MHz,  $\sqrt{\gamma_1}/(2\pi) = 0.128$  MHz, and  $\sqrt{\gamma_2}/(2\pi) = 0.214$  MHz. The  $\omega^\pm(k_1)$  bands are independently reproduced by the electric-circuit picture [see Eq. (A1) in Appendix A1, with  $C = 0.103$  nF,  $C_s = 0.552$  nF,  $C_1 = 0.0348$  nF, and

337  $C_2 = 0.116$  nF obtained by a best fitting procedure], also  
 338 in accordance with the above tight-binding model.

339 A more careful look at the potential field functions at  $\Gamma$   
 340 point plotted within the unit cell (see top panel of Fig. 4)  
 341 reveals a bonding ( $\Phi_+ = C_+(\phi_1 + \phi_2)$ ) and antibonding  
 342 ( $\Phi_- = C_-(\phi_1 - \phi_2)$ ) character in analogy with a diatomic  
 343 molecule picture in quantum physics,  $\phi_1$  and  $\phi_2$  being the  
 344 two atomic potential functions and  $C_{\pm}$  appropriate coeffi-  
 345 cients. Along  $\Gamma X$  direction the potential fields evolve  
 346 progressively towards a more weighted one-atom picture  
 347 with a double-degenerate state at X point (see two right  
 348 plots of the top panel in Fig. 4), this degeneracy being  
 349 lifted when inversion symmetry disappears ( $L_1 \neq L_2$ ).

350 This picture is further modified when piezoelectric cou-  
 351 pling is taken into account ( $e_{ij} \neq 0$ ), as it should be in  
 352 a real system. The result of our calculation is shown in  
 353 Fig. 4(b). As a first remark, one observes a blue shift  
 354 for the Lamb guided modes and a red shift for the EM  
 355 origin resonant bands. And more importantly, the two  
 356 eigenmode subspaces interact between each other and, in  
 357 general, one expects the formation of avoided crossings  
 358 between modes of the same symmetry. The lower in fre-  
 359 quency EM resonant band  $\omega^-(k_1)$  interacts with both the  
 360  $S_0$  branch and the first folded  $A_0$  branch, and similarly  
 361 the higher in frequency EM band  $\omega^+(k_1)$  interacts with  
 362 both the  $A_1$  branch and the first folded  $S_0$  branch, thus  
 363 leading to narrow selective absolute gaps (yellow-shaded  
 364 regions). A slight detuning between  $L_1$  and  $L_2$  lowers  
 365 further the symmetry of the system (inversion is now in-  
 366 valid) thus resulting in interactions, though very weak,  
 367 between all bands [see Fig. 4(c)].

368 Next, we confirm the above predictions, by their experi-  
 369 mental verification. We measured the potential signal  
 370  $V(x_{1,n}, t)$  along the  $n = 2, 3, \dots, 48$  electrode positions  
 371 located at the upper side of the plate, and after appli-  
 372 cation of the AR2D model, we obtain the experimental  
 373  $V(\omega, k_1)$ , whose amplitude is shown in Fig. 5(a), and  
 374 close to it, in Fig. 5(b), the calculated frequency band  
 375 structure shown in Fig. 4(b). The different branches are  
 376 color-indexed with the value of the potential, averaged on  
 377 the area of the upper-side electrodes: the darker the tra-  
 378 jectory, the weaker the electromechanical coupling, that  
 379 takes place within the plate, is.

380 The experimental dispersion plot mainly reveals the  
 381  $S_0$ -like branches of positive slope in the positive part  
 382 of the 1<sup>st</sup> and negative part of the 2<sup>nd</sup> BZ, that com-  
 383 pare well to the corresponding theoretical curve with effec-  
 384 tive medium slope of  $3013$  m s<sup>-1</sup> at the long wave-  
 385 length limit. In addition, one observes some bright spots  
 386 spanning the frequency region between  $0.6$  and  $0.7$  MHz,  
 387 that could correspond to the localized modes of EM  
 388 origin in Fig. 5(b) at about  $0.58$  MHz for  $\omega^-(k_1)$  and  
 389 at about  $0.67$  MHz for  $\omega^+(k_1)$ . At higher frequencies  
 390 but below  $1$  MHz, two more trajectories are experi-  
 391 mentally observed, belonging probably to  $A_1$ -like and  $S_0$ -like  
 392 branches, visible in the positive part of the 1<sup>st</sup> and 2<sup>nd</sup>  
 393 BZ, respectively (but also in the negative part of the 2<sup>nd</sup>  
 394 and 1<sup>st</sup> BZ). The comparison between theory and experi-

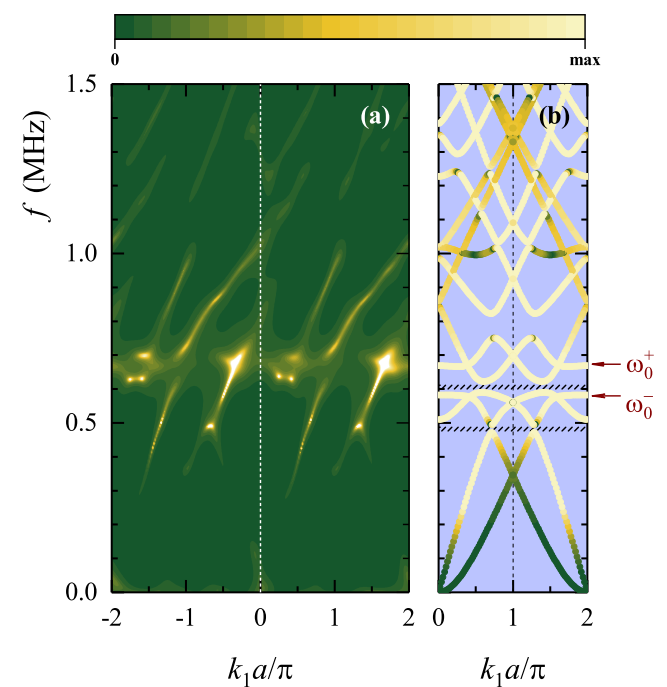


FIG. 5. Frequency band structure of the diatomic grounded- $L$  piezoelectric phononic crystal (lattice constant  $a = 2a_0 = 2$  mm) with EBCs depicted in Fig. 3(a). (a) Experimental dispersion plot for the finite crystal, consisting of  $N = 24$  unit cells, obtained by use of the AR2D model on the electric-potential signal recorded at the upper-side electrode positions. (b) Calculated dispersion plot obtained through finite-element numerical simulations for the corresponding infinite crystal for  $L = 30$   $\mu$ H. In (a) the color map is saturated; in (b) the trajectories are color-indexed with the average potential on the upper-side electrodes of the unit cell. Red arrows and hatched areas denote, respectively, frequency bounds of the EM bands at  $\Gamma$  point and absolute gaps.

395 ment is, however, not straightforward, especially because  
 396 the finite-element simulations predict much more active  
 397 branches than seen experimentally.

### 398 B. Floating potential and inductance loaded two-atom 399 unit cell

400 If we replace the two grounded ends of the previous  
 401 structure by free floating potential (FP) ends, we obtain  
 402 the unit cell shown in Fig. 3(b). A similar methodol-  
 403 ogy can be developed as that given in Sec. III A in order  
 404 to follow the formation of the resonant bands; the main  
 405 difference lies in the specific form of this band before hy-  
 406 bridization. As it can be easily shown<sup>31</sup> this branch is  
 407 hyperbolic for the corresponding monatomic crystal [con-  
 408 sider only the left half part of the unit cell of Fig. 3(b)]  
 409 and when constructing the diatomic unit cell, the fold-  
 410 ing results in two branches, one hyperbola-like,  $\omega^+(k_1)$ ,  
 411 extended in frequency, the other,  $\omega^-(k_1)$ , relatively flat.  
 412 When  $L_1 = L_2$  these two distinct bands degenerate to

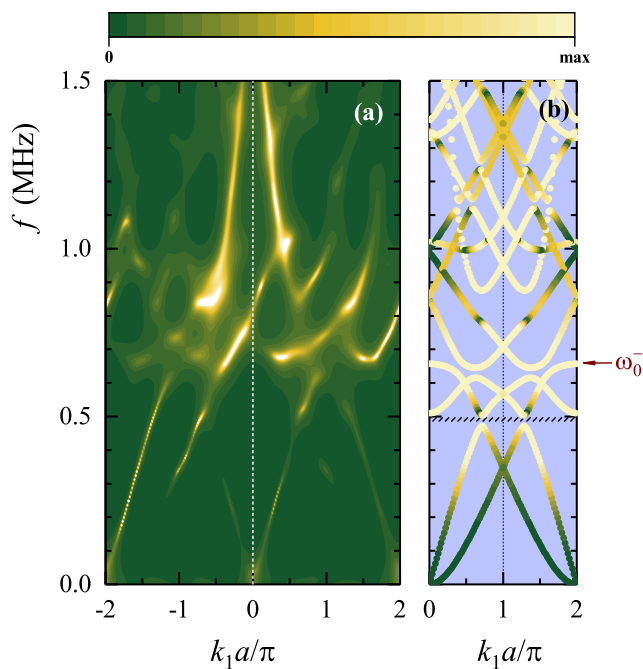


FIG. 6. Frequency band structure of the floating-potential- $L$  piezoelectric phononic crystal (lattice constant  $a = 2a_0 = 2$  mm) with EBCs depicted in Fig. 3(b). (a) Experimental dispersion plot for the finite crystal, consisting of  $N = 24$  unit cells, obtained by use of the AR2D model on the electric-potential signal recorded at the upper-side electrode positions. (b) Calculated dispersion plot obtained through finite-element numerical simulations for the corresponding infinite crystal for  $L = 30 \mu\text{H}$ . In (a) the color map is saturated; in (b) the trajectories are color-indexed with the average potential on the upper-side electrodes of the unit cell. Red arrow and hatched area denote, respectively, frequency bounds of the EM band at  $\Gamma$  point and absolute gap.

413 a common frequency  $\omega_\pi$  at X point; again this degeneracy  
 414 originating from the inversion symmetry of the unit  
 415 cell, is lifted if  $L_1 \neq L_2$ . The finite frequency point  
 416  $\omega_0^- = \omega^-(k_1 = 0)$  can be tuned through the choice of  $L$ .  
 417 Analytic expressions are derived in terms of an equivalent  
 418 periodic transmission-line picture, as detailed in Ap-  
 419 pendix A 2.

420 The experimental frequency band structure of our  
 421 finite-size sample is obtained following the same pro-  
 422 cedure, as for the previous case of grounded crystal  
 423 (Sec. III A). The results are shown in Fig. 6(a), and next  
 424 to it [Fig. 6(b)] the calculated frequency band structure  
 425 for the corresponding infinite crystal, assuming again a  
 426 pure  $L$ -component ( $L = 30 \mu\text{H}$ ). In the experimental  
 427 picture, three frequency regions are distinguished: be-  
 428 low 0.6 MHz the  $S_0$ -like and  $A_0$ -like branches are clearly  
 429 identified, in good agreement with those predicted theo-  
 430 retically, and this was also the case for the grounded  
 431 crystal (Fig. 5). Next, for frequencies above 0.6 MHz  
 432 and below 1.0 MHz some bright spots are observed but a  
 433 one-to-one comparison to the theoretical picture becomes

434 not straightforward. Finally, above 1.0 MHz the two ex-  
 435 tended, hyperbolic branches become dominant and are  
 436 clearly observed within the 1<sup>st</sup> BZ, in both its positive  
 437 and negative part.

438 In both cases examined up to now, we remark that the  
 439 experimental dispersion plots [Figs. 5(a) and 6(a)] do not  
 440 reveal all branches predicted theoretically, and, more im-  
 441 portantly, symmetry operations such as translation sym-  
 442 metry by a reciprocal lattice vector,  $\omega(k_1) = \omega(k_1 + \frac{2\pi}{a})$ ,  
 443 and/or mirror symmetry,  $\omega(k_1) = \omega(-k_1)$ , are not ob-  
 444 served for all trajectories. This could be explained by  
 445 finite size effects and excitation that favors some of the  
 446 branches with respect to others. To facilitate compari-  
 447 son to the theoretical picture, we artificially restore the  
 448 above said lost symmetries, by taking the average on the  
 449 positive- $k_1$  and negative- $k_1$  part after, i) horizontal flip-  
 450 ping, and, ii) horizontal translation by 2 (in reduced  $k_1$ -  
 451 axis units) of the latter. These two operations lead to  
 452 a picture with mirror symmetry with respect to vertical  
 453 (frequency) axis at both  $\Gamma$  and X points, thus the  $\Gamma\text{X}$   
 454 direction is sufficient for any analysis. The results are  
 455 shown in Fig. 7, for the grounded crystal [left panel, plot  
 456 (a)] and for the floating-potential crystal [right panel,  
 457 plot (c)]. Their comparison to the corresponding theo-  
 458 retical predictions [Figs. 5(b) and 6(b)] reveals a red shift  
 459 of the simulated EM modes. Obviously, the reality, far  
 460 away from the numerous simplifications assumed in the  
 461 simulations, includes finite size effects, different elastic  
 462 boundary conditions at the edges of the plate due to the  
 463 use of the PCI cards, and, real-electronics effects, present  
 464 in the circuitry, that were neglected in the previous analy-  
 465 sis. In fact, a  $Z_e$  impedance load (see Appendix B) will be  
 466 considered instead of the idealized  $Z^u = Z^d = Z_L = iL\omega$   
 467 generated by a pure  $L$ -component. In plots (b) and (d)  
 468 of Fig. 7 we show the calculated band structures that  
 469 correspond to those of Figs. 5(b) and 6(b), but for the  
 470 real load  $Z_e$  [Eq. (B1)] instead of the pure inductive load  
 471 with  $L = 30 \mu\text{H}$ . The use of  $Z_e$  blue-shifts the EM  
 472 modes [by about  $\sim 10\%$  for  $\omega_0^\pm$  with respect to those  
 473 of Figs. 5(b) and 6(b), indicated here by red arrows as  
 474 guides to the eye] and improves the comparison between  
 475 experimental data and theoretical simulations. The EM  
 476 modes manifest themselves as two flat bands lying in the  
 477 frequency range from 0.6 to 0.75 MHz for the grounded-  
 478  $L$  crystal [Fig. 7(b)] in rather good agreement with the  
 479 experimental picture [bright spots extending from 0.63  
 480 to 0.71 MHz in Fig. 7(a)]. For the floating-potential- $L$   
 481 crystal [Fig. 7(d)] the EM modes manifest themselves, on  
 482 the one hand, as a flat band centered at 0.7 MHz and, on  
 483 the other hand, as a hyperbolic branch which interacts  
 484 strongly with the  $A_1$ -like branch and spans the whole  
 485 frequency range above 0.9 MHz; these compare well to  
 486 the experimental picture [Fig. 7(c)] that reveals, respec-  
 487 tively, a flat bright segment from 0.66 to 0.75 MHz and  
 488 a hyperbolic branch above 0.82 MHz.

489 We note in passing the appearance of narrow, selective,  
 490 absolute frequency gaps for both systems [see hatched ar-  
 491 eas in Figs. 7(b), (d)] originating from avoided-crossing



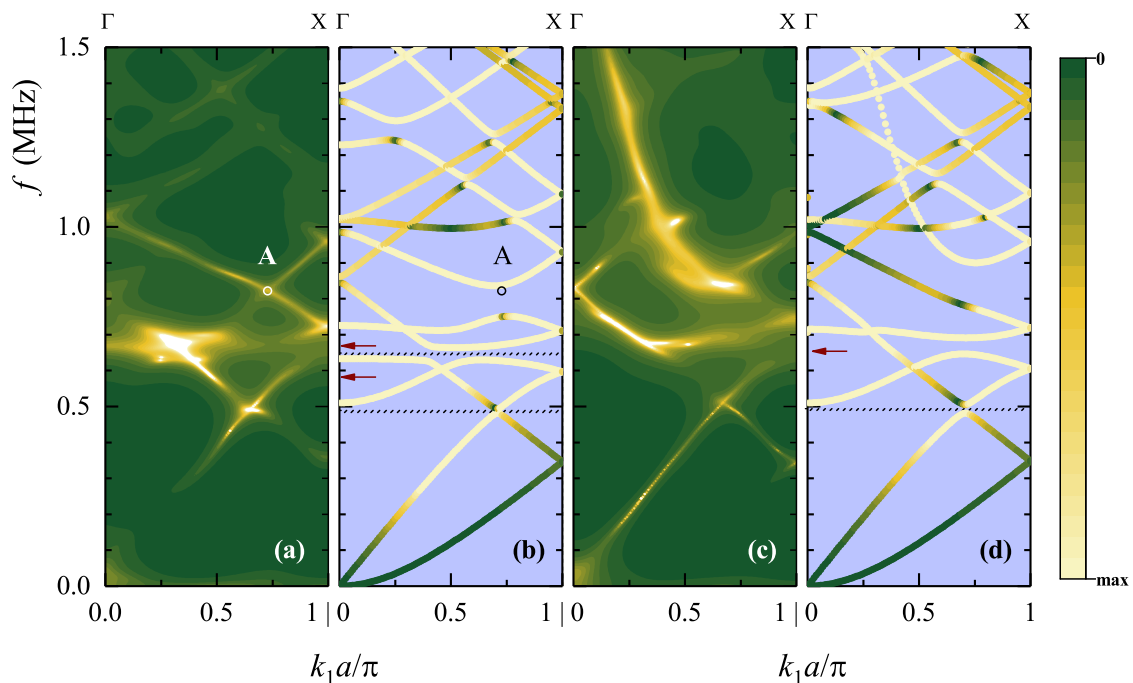


FIG. 7. Experimental frequency band structure of the diatomic (a) grounded- $L$  and (c) floating-potential- $L$  piezoelectric phononic crystals, after reduction along  $\Gamma X$  direction (see text) of their initial map plots, shown respectively in Figs. 5(a) and 6(a). In (b) and (d) the corresponding calculated dispersion plots for the infinite crystals, assuming real loads  $Z_e$  instead of the pure inductive ones  $Z_L$  ( $L = 30 \mu\text{H}$ ). Red arrows denote the frequency positions of the EM bands at  $\Gamma$  point as predicted for the case of  $Z_L$  instead of  $Z_e$  [see Figs. 5(b) and 6(b), respectively]; hatched areas indicate, as usually, absolute gaps.

492 between bands of the same symmetry. Therefore, one ex-  
 493 pects that even structures with a small number of units  
 494 will exhibit such type of gaps<sup>32</sup>. Their frequency po-  
 495 sition is indirectly controlled through  $\omega_0$  values scaling  
 496 as  $\sim L^{-1/2}$  [see Appendix A]. Their width is narrow,  
 497 but possible enlargement could be achieved with elec-  
 498 tronic components facilitating the degree of interaction  
 499 [e.g., negative capacitors<sup>25</sup>].

500 A careful global evaluation of the picture obtained by  
 501 both models used for the simulations, i.e.,  $Z_L$  and  $Z_e$ ,  
 502 for the two crystals under study, suggests that none of  
 503 these can perfectly describe the experimental picture in  
 504 terms of frequency position of the EM modes (they are in  
 505 general slightly shifted, but the hyperbolic branch clearly  
 506 blue-shifted in the simulations) and in terms of degree of  
 507 interaction that takes place in the avoided-crossing re-  
 508 gions when EM and Lamb-like modes cross each other  
 509 [weak avoiding is experimentally observed, while a strong  
 510 one is predicted, e.g. at point A in Figs. 7(a), (b)].  
 511 Deviations are also observed between some dark branch  
 512 segments (vanishing potential value along them), while  
 513 predicted highlighted in theory, e.g., the  $A_1$ -like branch  
 514 which is theoretically predicted with a cut-off frequency  
 515 close to 0.5 MHz is not experimentally discernible. We  
 516 deduce that even if a pure  $L$ -component is too simple  
 517 to reproduce exactly the experimental picture of the dis-  
 518 persion plot of these crystals, the use of the experimen-  
 519 tally identified load  $Z_e$  is not sufficient either. A possible

520 reason could be the modification of this individual-atom  
 521 load  $Z_e$  (we recall that its identification has been real-  
 522 ized under isolated conditions, outside the crystal) when  
 523 it is introduced in our device including the plate itself  
 524 and the system of two PCI cards. On the other hand,  
 525 simulations still constitute idealized models, since they  
 526 neglect any finite size effects and leakage of elastic and  
 527 EM modes in the surrounding medium (air). For the  
 528 above reasons, comparison between theory and exper-  
 529 iments remains, however, very satisfactory and provides  
 530 a good verification of the main features of the dispersion  
 531 properties of these crystals.

### 532 C. Intercellular inductance loaded unit cell

533 As a last case, we examine a crystal plate with inter-  
 534 cellular connection of adjacent strips located at the same  
 535 side of the plate (say the upper one) via an inductance  
 536 load  $L$ , the other-side strips being grounded, as depicted  
 537 in Fig. 3(c). These EBCs conserve the periodicity of the  
 538 metallic array. The numerically predicted band struc-  
 539 ture of that crystal (lattice constant  $a = a_0$ ) is shown in  
 540 Fig. 8 for two distinct inductance values:  $L = 150 \mu\text{H}$   
 541 [plot (a)] and  $L = 30 \mu\text{H}$  [plot (b)]. The most striking  
 542 feature of these dispersion plots is the appearance of a  
 543 linear-dispersion branch at the long-wavelength limit,  
 544 in addition to the traditionally expected  $S_0$ -like and  $A_0$ -like

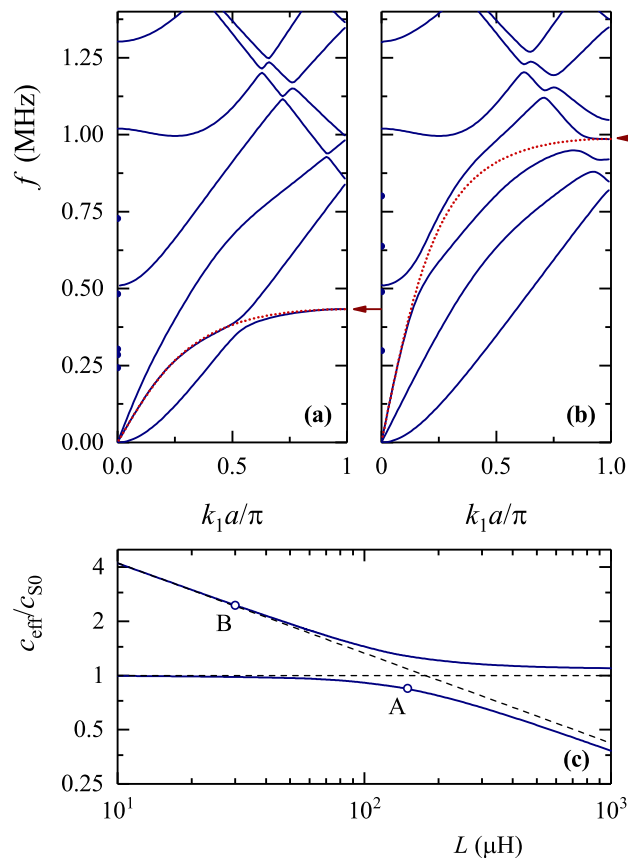


FIG. 8. Calculated frequency band structure for a monoatomic crystal of lattice constant  $a = a_0$  whose unit cell is depicted in Fig. 3(c) with (a)  $L = 150 \mu\text{H}$  and (b)  $L = 30 \mu\text{H}$ . The dotted red lines represent an estimate of the unhybridized  $L$ -induced band, applying Eq. (A3) for appropriate values of the parameters  $C$ ,  $C_s$  (see text), with starting parameters  $\omega_\pi / (2\pi)$  (indicated by red arrows) and the long-wavelength slope,  $c_{\text{eff}}$ , of this frequency branch. (c) Evolution of the slope of the two linear branches at  $\omega \rightarrow 0$  for several values of the inductance load  $L$ . Horizontal and oblique dashed lines represent, respectively, the effective medium slope of the  $S_0$  branch of the corresponding grounded crystal and the  $L$ -induced branch from Eq. (A3) calculated for  $C$ ,  $C_s$  determined for  $L = 10 \mu\text{H}$ . Points A and B correspond to the  $L$ -induced bands (red dotted curves) of plots (a) and (b), respectively.

545 branches emerging at the same frequency range. The gen-  
 546 eral form of that  $L$ -induced branch when the piezoelectric  
 547 coupling is switched off ( $e_{ij} = 0$ ) follows the schematic  
 548 representation given in the right plot of Fig. 3(c) and  
 549 is described by the relation (A3) for some appropriate  
 550 values  $C$ ,  $C_s$  in an equivalent periodic transmission line  
 551 picture. The slope,  $c_{\text{eff}}$ , of this  $L$ -branch is tuned via  
 552 the choice of  $L$ , and covers a wide range of effective  
 553 medium velocities not easily encountered in ordinary mat-  
 554 erials. The equivalent transmission line model presented  
 555 in Appendix A predicts a scaling  $\sim L^{-1/2}$  for given ( $L$ -  
 556 independent)  $C$  and  $C_s$  values (we find  $C = 0.645 \text{ nF}$  and  
 557  $C_s = 0.593 \text{ nF}$ , for the crystal under study). When this

558 coupling is switched on ( $e_{ij} \neq 0$ ), as it should be in a real  
 559 system, the  $L$ -induced band interacts with the same sym-  
 560 metry bands of Lamb eigenmodes and generates avoided-  
 561 crossing effects. To facilitate its visualization before hy-  
 562 bridization, we apply the same relation [Eq. (A3), with  
 563 different values of  $C$ ,  $C_s$ , reflecting all coupling effects] to  
 564 model its unhybridized form, represented in Fig. 8(a) and  
 565 (b) by red dotted lines: after a careful reading of these  
 566 dispersion plots, we identify the two starting parameters,  
 567  $\omega_\pi$  (indicated by a red arrow), and,  $c_{\text{eff}}$ , the effective-  
 568 medium slope of this branch at the long-wavelength limit,  
 569 used to deduce the internal model capacitance paramet-  
 570 ers ( $C = 0.737 \text{ nF}$  and  $C_s = 0.868 \text{ nF}$ , for  $L = 30 \mu\text{H}$ ;  
 571  $C = 1.413 \text{ nF}$  and  $C_s = 0.900 \text{ nF}$ , for  $L = 150 \mu\text{H}$ ).

572 For the case of  $L = 150 \mu\text{H}$  [Fig. 8(a)], the  $L$ -  
 573 band with  $c_{\text{eff}} = 2560 \text{ m s}^{-1}$  interacts weakly with the  
 574  $A_0$ -like branch, and a small avoided-crossing occurs at  
 575 about 0.375 MHz; the other linear,  $S_0$ -like, branch has  
 576  $c_{\text{eff}} = 3850 \text{ m s}^{-1}$ , which is higher than the correspond-  
 577 ing value in a grounded crystal,  $c_{S_0} = 3020 \text{ m s}^{-1}$ . For  
 578 the case of  $L = 30 \mu\text{H}$  [Fig. 8(b)], the  $L$ -band with  
 579  $c_{\text{eff}} = 7400 \text{ m s}^{-1}$  interacts weakly with the  $A_1$ -like  
 580 branch as well as with the first folded  $A_0$ -like branch,  
 581 giving rise to relatively larger avoided crossings, occur-  
 582 ring, respectively, at about 0.50 MHz and 0.95 MHz;  
 583 the other linear,  $S_0$ -like, branch has  $c_{\text{eff}} = 2970 \text{ m s}^{-1}$ ,  
 584 which is lower than  $c_{S_0}$ . The above suggest a possible  
 585 interaction with the  $S_0$ -like branch when the two modes  
 586 are close enough. In Fig. 8(c) we plot the evolution of  
 587 the slope at the long-wavelength limit, for several val-  
 588 ues of the inductance covering a large range spanning  
 589 over two orders of magnitude, of both linear branches  
 590 of a typical dispersion plot as those shown in Fig. 8(a)  
 591 and (b). One clearly observes a hybridization between  
 592 two distinct modes: the  $S_0$ -like mode, represented by the  
 593 horizontal dashed line, and the  $L$ -induced mode, repre-  
 594 sented by the oblique dashed line that corresponds to  
 595 the  $\sim L^{-1/2}$  scaling rule calculated at  $L = 10 \mu\text{H}$  (for  
 596  $C / [1 + C / (4C_s)] = 0.618 \text{ nF}$ ), far away from the crossing  
 597 point that occurs in the vicinity of  $L = 150 \mu\text{H}$ . For this  
 598 value of  $L$ , a high-degree hybridization takes place, both  
 599 linear-dispersion modes carry both the  $S_0$  and  $L$ -induced  
 600 character, the point A corresponding to the  $L$ -induced  
 601 band. On the contrary, for  $L = 30 \mu\text{H}$  point B, that  
 602 corresponds to the  $L$ -induced band, conserves mainly its  
 603  $L$ -induced character.

604 We turn now our attention to the comparison with  
 605 experimental results. As previously, the  $Z_e$  load will  
 606 be considered instead of the idealized  $Z_L$  in the cal-  
 607 culations. We measured the potential signal along the  
 608  $n = 2, 3, \dots, 48$  electrode positions located at the up-  
 609 per side of the plate, and after application of the AR2D  
 610 model, we obtain the experimental  $V(\omega, k_1)$  whose am-  
 611 plitude is shown in Fig. 9(a) that compares well with the  
 612 calculated frequency band structure including the real  
 613 load  $Z_e$ , in Fig. 9(b).

614 The linear-slope, effective-medium branch of EM ori-  
 615 gin, clearly observed in the experiments, is perfectly re-

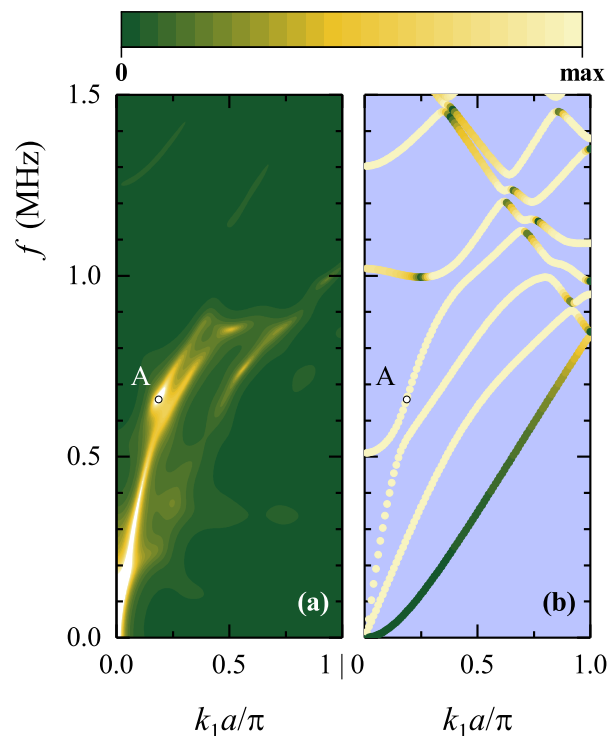


FIG. 9. (a) Experimental and (b) calculated frequency band structure for the monoatomic crystal of lattice constant  $a = a_0$  whose unit cell is depicted in Fig. 3(c), loaded with impedance  $Z_e$  [Eq. (B1)]. In (b) the dispersion lines are color-indexed with the projection of the potential value averaged in the upper-side electrode of the unit cell.

616 produced in the calculations. The same holds for the  
 617 bright part of the  $A_1$ -like branch [see point A in Fig. 9(a)],  
 618 though the latter is not discernible experimentally close  
 619 to its cut-off frequency at  $\sim 0.5$  MHz (this was also  
 620 the case for the crystals presented in Sec. III A and  
 621 III B). The  $S_0$ -like branch is also observed experimen-  
 622 tally, though with lower amplitude than predicted in the  
 623 theoretical calculation. We note that the latter fails to  
 624 capture the degree of repulsion of the trajectories in the  
 625 vicinity of point A and for frequencies above it (this  
 626 avoiding is predicted to be larger than experimentally  
 627 observed). We close this part by a general remark con-  
 628 cerning the  $A_0$ -like branch which is not observed (apart  
 629 some slightly visible parts close to X point), since the po-  
 630 tential takes very low values along it, in all cases studied  
 631 here, in perfect agreement with our numerical calcula-  
 632 tions.

#### 633 IV. CONCLUSIONS

634  
 635 In conclusion, we have presented a thorough analy-  
 636 sis of the dispersion properties of piezoelectric phononic  
 637 plates, structured with metallic arrays on their surfaces

638 and loaded with inductive circuits. These structures,  
 639 studied experimentally and theoretically, exhibit a va-  
 640 riety of localized and/or extended in frequency modes  
 641 that originate from an electric circuit behavior related to  
 642 the inductive loads and span the low, intermediate, or  
 643 high frequency range in a typical dispersion plot. This  
 644 low-pass, band-pass, and high-pass behavior that mani-  
 645 fests itself as an important potential variation along these  
 646 trajectories, combined to the automatized, controllable  
 647 character of our experimental device, constitute a power-  
 648 ful tool for applications targeting real-time manipulation  
 649 of elastic waves via EM waves and vice-versa. We demon-  
 650 strate the appearance of unusual, high-valued, positive or  
 651 negative group-velocity branches, not encountered in typ-  
 652 ical Lamb-like dispersion plots of phononic plates, easily  
 653 tuned via the external inductive loads.

654 Our experimental results, enhanced by non-ordinary,  
 655 high-resolution signal processing techniques, are in ac-  
 656 cordance with the theoretical predictions —despite some  
 657 isolated discrepancies; they confirm the basic underlying  
 658 mechanisms analyzed in this paper and the main phe-  
 659 nomenological aspects that interest us for applications, our  
 660 aim being among others the realization of viable, simple  
 661 devices that can operate under real conditions and pro-  
 662 duce the desired effects in the modulation of the disper-  
 663 sion properties of these crystals. Nevertheless, although  
 664 its very application-oriented aspect at a first sight, this  
 665 study councils *per se* an important physical insight.

#### 666 DATA AVAILABILITY STATEMENT

667 The data that support the findings of this study are  
 668 available from the corresponding author upon reasonable  
 669 request.

#### 670 Appendix A: Equivalent electric circuits

671 A piezoceramic plate with metallized surfaces can be  
 672 effectively described by an equivalent capacitor. When  
 673 metallic strips are structured periodically on its both sur-  
 674 faces, we can use an equivalent picture of a periodic trans-  
 675 mission line whose unit cell coincides with the unit cell of  
 676 the real structure. We give in what follows the electric-  
 677 circuit models that correspond to such a description for  
 678 the cases studied in this paper.

#### 679 1. Two-atom grounded- $L$ crystal

680 The equivalent circuit that models the two electric res-  
 681 onators shown in Fig. 3(a) when the piezoelectric cou-  
 682 pling is switched off is depicted in Fig. 10(a). We define  
 683 all voltages in the input,  $V_{A_j}$ , and output,  $V_{B_j} = \mathcal{P}V_{A_j}$ ,  
 684 of the unit cell with respect to a common ground refer-  
 685 ence, where  $j = 1, 2$ , and  $\mathcal{P} = e^{-ik_1 a}$  is the Bloch phase  
 686 factor (we assume an  $e^{+i\omega t}$  time dependance in all fields);

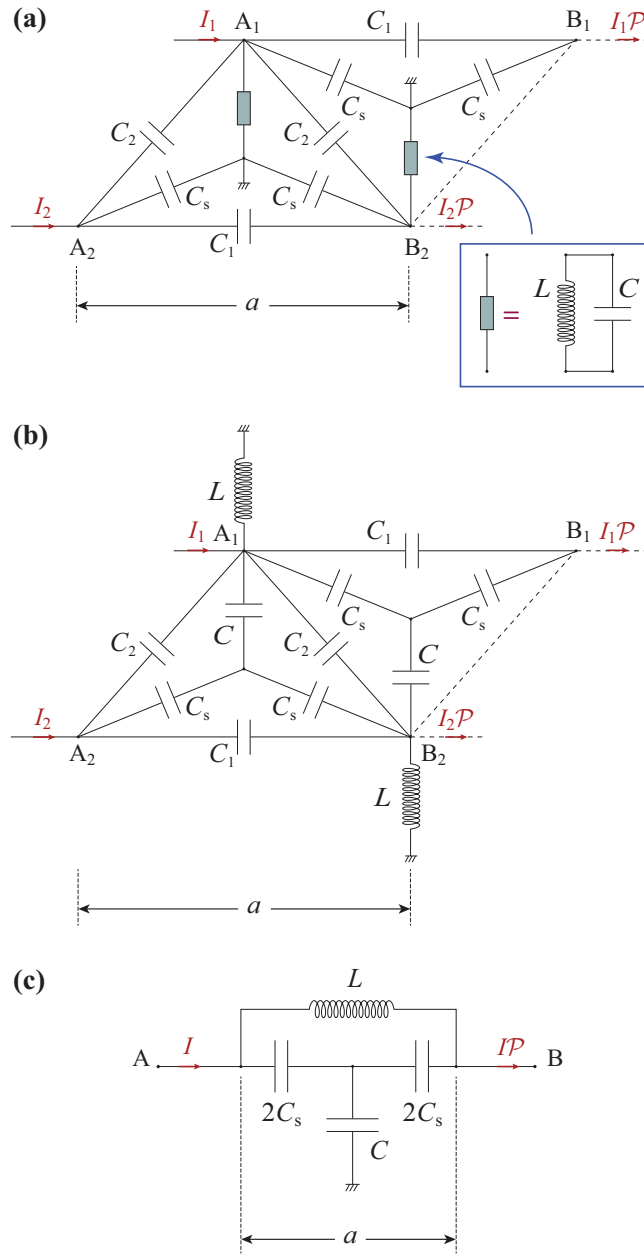


FIG. 10. The unit cell of a periodic transmission line describing equivalently (a) the two-atom grounded- $L$  crystal [Fig. 3(a)], (b) the two-atom floating-potential- $L$  crystal [Fig. 3(b)], and (c) the intercellular- $L$  crystal [Fig. 3(c)], when electromechanical coupling is switched off.

687 the incoming and outgoing electric currents are respectively  $I_j$  and  $\mathcal{P}I_j$ . Application of Kirchhoff's current and  
688 voltage laws leads to a secular equation depending only  
689 on  $\mathcal{P}$  and the set of unit-cell impedances. We thus obtain  
690 the following dispersion equation for the two electric  
691 resonant bands  
692

$$\omega^\pm(k_1) = \left[ LC \left( 1 + 2 \frac{C_s + C_1 + C_2}{C} \right) \right. \quad (\text{A1})$$

$$\left. - 2 \frac{C_1}{C} \cos k_1 a \mp 2 \frac{C_2}{C} \cos \frac{k_1 a}{2} \right]^{-1/2}.$$

693 At  $\Gamma$  point (center of the BZ) the two distinct eigen-  
694 frequencies are  $\omega_0^+ = [LC(1 + 2\frac{C_s}{C})]^{-1/2}$  and  $\omega_0^- =$   
695  $[LC(1 + 2\frac{C_s + 2C_2}{C})]^{-1/2}$ , corresponding to a *bonding* and  
696 an *antibonding* mode; at X point (edges of the BZ) a  
697 double degenerate eigenfrequency is found to be  $\omega_\pi =$   
698  $[LC(1 + 2\frac{C_s + 2C_1 + C_2}{C})]^{-1/2}$ . The width  $\Delta\omega^\pm = |\omega_0^\pm -$   
699  $\omega_\pi|$  of these cos-like resonant bands is finite, and controlled  
700 by  $L$  and the internal effective parameters of the model  
701  $C$ ,  $C_s$ ,  $C_1$  and  $C_2$ . We note that these capacitors  
702 do not correspond to real electronic elements in our device,  
703 but they describe its equivalent behavior.  $C$  and  $C_s$   
704 account for a capacitive effect between electrodes located  
705 at the two opposite sides (i.e., along  $x_3$ -direction) and at  
706 the same side (i.e., along  $x_1$ -direction) of the plate, respectively.  
707  $C_1$  and  $C_2$  describe the capacitive interaction  
708 between electrodes of the same side at distance  $a = 2a_0$   
709 and between electrodes at the opposite sides at distance  
710  $R = \sqrt{a_0^2 + h^2}$ , respectively, in one-to-one analogy with  
711 the overlapping coefficients  $\gamma_1$ ,  $\gamma_2$  of the tight-binding  
712 model.

## 713 2. Two-atom floating-potential- $L$ crystal

714 For the case of the two-atom crystal with an alternation  
715 of floating-potential EBCs and inductance loads —  
716 its unit cell is given in Fig. 3(b)— we proceed in a similar  
717 manner to construct its equivalent circuit [see Fig. 10(b)]  
718 that models the two electric resonators. Using the same  
719 steps as for the previous case, we obtain, after a relatively  
720 lengthy but straightforward algebra, the following  
721 dispersion equation for the two electric bands

$$\omega^\pm(k_1) = \left\{ 2LC \left[ \frac{C_1 + 2C_2}{C} + \frac{C_s}{C} \frac{2C + C_s}{C + 2C_s} \right. \quad (\text{A2}) \right. \\ \left. - \left( \frac{C_1}{C} + \frac{C_s}{C} \frac{C_s}{C + 2C_s} \right) \cos k_1 a \right. \\ \left. \mp 2 \left( \frac{C_2}{C} + \frac{C_s}{C + 2C_s} \right) \cos \frac{k_1 a}{2} \right] \right\}^{-1/2}.$$

722 At  $\Gamma$  point two distinct eigensolutions are found, one fi-  
723 nite  $\omega_0^- = [8LC_2(1 + \frac{C}{C_2} \frac{C_s}{2C_s + C})]^{-1/2}$  and one diverg-  
724 ing as  $\omega_0^+ \sim [LC_1(1 + \frac{C_s}{C_1} \frac{C_s}{2C_s + C})]^{-1/2} (k_1 a)^{-1}$ . The  
725 higher frequency branch  $\omega^+(k_1)$  behaves as an hyper-  
726 bolic function for  $k_1 a \ll 1$ , while the lower frequency  
727 branch  $\omega^-(k_1)$  corresponds to a cos-like resonant band  
728 of finite width  $\Delta\omega^- = |\omega_0^- - \omega_\pi|$ , where  $\omega_\pi$  is the com-  
729 mon, double degenerate eigenfrequency at X point, found  
730 to be  $\omega_\pi = [4L(C_1 + C_2 + C_s \frac{C + C_s}{C + 2C_s})]^{-1/2}$ . The form  
731 of these two dispersive modes is still controlled by  $L$  and  
732 the internal effective parameters of the model  $C$ ,  $C_s$ ,  $C_1$

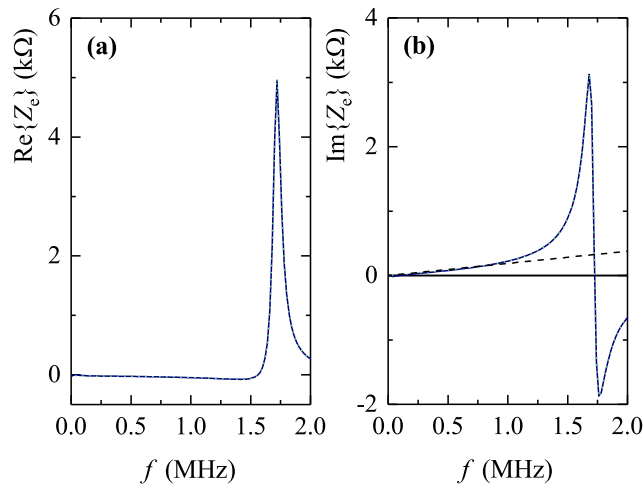


FIG. 11. Real (a) and imaginary (b) part of the impedance load  $Z_e$  used in the external circuits of Fig. 3. Solid and dotted lines represent the real (measured) and modeled [Eq. (B1)] function, respectively; in (b) the impedance of a pure inductance  $L = 30 \mu\text{H}$  is also shown (broken line) for comparison.

733 and  $C_2$ , whose physical meaning is the same as that for  
734 the grounded- $L$  crystal.

### 735 3. Intercellular- $L$ crystal

736 The unit cell of Fig. 3(c) is modeled by the periodic  
737 transmission line whose unit cell is shown in Fig. 10(c).  
738 We easily obtain the following dispersion relation

$$\begin{aligned} \omega(k_1) &= \omega_0 \left[ \frac{C}{4C_s} + \left( 2 \sin \frac{k_1 a}{2} \right)^{-2} \right]^{-1/2}, \\ \omega_0 &= \left[ \frac{1}{LC} \left( 1 + \frac{C}{4C_s} \right) \right]^{1/2} \end{aligned} \quad (\text{A3})$$

739 from which one can immediately deduce the angular fre-  
740 quency at X point,  $\omega_\pi = \frac{1}{\sqrt{LC_s}}$ , and the effective medium  
741 velocity at the long wavelength limit  $c_{\text{eff}} = \lim_{k_1 \rightarrow 0} \frac{\omega}{k_1} =$   
742  $a\omega_0$ . In this simplified but still quite accurate model,  
743 knowledge of two external parameters, e.g.  $\omega_\pi$  and  $\omega_0$   
744 (or, equivalently,  $c_{\text{eff}}$ ), is sufficient to determine the in-  
745 ternal model parameters,  $C$  and  $C_s$ .

### 746 Appendix B: Impedance-load function

747 The external impedance load is ideally assumed to be  
748 an inductance  $L$  connected to the metallic strips, as de-  
749 tailed in Fig. 3. However, in practice, the real compo-  
750 nent, used in our experiments, has not a pure inductive  
751 behavior; other contributions have to be taken into ac-  
752 count, related to several internal circuitry parts of re-  
753 sistive and/or capacitive type of this component. The  
754 measured impedance  $Z_e$  of our individual component — a

755 representative one, extracted from the crystal— is plot-  
756 ted in Fig. 11 against frequency,  $f$ , and both its real and  
757 imaginary parts [plots (a) and (b), respectively] show a  
758 resonant behavior at about 1.71 MHz. Within the fre-  
759 quency range that interest us here (up to 2 MHz) this  
760 function can be in a very good approximation described  
761 by the following rational expression

$$\begin{aligned} Z_e &= \frac{\alpha_4 f^4 + \alpha_3 f^3 + \alpha_2 f^2 + \alpha_1 f + \alpha_0}{f^2 + \beta_1 f + \beta_0} \quad (\text{B1}) \\ &= \gamma_0 + \gamma_1 f + \gamma_2 f^2 + \frac{\delta_+}{f - f_+} + \frac{\delta_-}{f - f_-} \end{aligned}$$

762 where  $f$  is expressed in MHz in the above expressions,  
763 and  $\alpha_n$  and  $\beta_n$  are appropriate complex coefficients ob-  
764 tained by a fitting procedure

$$\begin{aligned} \alpha_4 &= -5.15566 - i5.18013 \times 10^{-14}, \quad (\text{B2}) \\ \alpha_3 &= -6.96706 \times 10^{-14} + i22.0970, \\ \alpha_2 &= 52.4644 + i4.78721 \times 10^{-13}, \\ \alpha_1 &= 4.56112 \times 10^{-13} - i452.779, \\ \alpha_0 &= 56.4767 - i7.41831 \times 10^{-13}, \\ \beta_1 &= -7.61040 \times 10^{-17} - i0.0790166, \\ \beta_0 &= -2.94215 + i8.96296 \times 10^{-18}, \end{aligned}$$

765 and

$$\begin{aligned} \gamma_0 &= \alpha_2 - \alpha_3 \beta_1 + \alpha_4 (\beta_1^2 - \beta_0) \quad (\text{B3}) \\ &= 35.5818 + i3.22798 \times 10^{-13}, \\ \gamma_1 &= \alpha_3 - \alpha_4 \beta_1 \\ &= -6.59699 \times 10^{-14} + i21.6896, \\ \gamma_2 &= \alpha_4, \\ \delta_\pm &= \pm 51.4400 - i193.077, \\ f_\pm &= \frac{1}{2} \left( -\beta_1 \pm \sqrt{\beta_1^2 - 4\beta_0} \right) \\ &= \pm 1.71481 + i0.0395083. \end{aligned}$$

766 <sup>1</sup>M. Leamy, M. Carrara, A. Erturk, M. Cacan, and M. Ruzzene,  
767 "Metamaterial-inspired structures and concepts for elastoacous-  
768 tic wave energy harvesting," *Smart Mater. Struct.* **22**, 065004  
769 (2013).

770 <sup>2</sup>J. Li, X. Zhou, G. Huang, and G. Hu, "Acoustic metamaterials  
771 capable of both sound insulation and energy harvesting," *Smart*  
772 *Mater. Struct.* **25**, 045013 (2016).

773 <sup>3</sup>L. Wu, Y. Wang, K. Chuang, F. Wu, Q. Wang, W. Lin, and  
774 H. Jiang, "A brief review of dynamic mechanical metamaterials  
775 for mechanical energy manipulation," *Mater. Today* **44**, 168–193  
776 (2021).

777 <sup>4</sup>Z. Liu, X. Zhang, Y. Mao, Y.Y. Zhu, Z. Yang, C.T. Chan, and  
778 P. Sheng, "Locally resonant sonic materials," *Science* **289**, 1734–  
779 1736 (2000).

780 <sup>5</sup>J. Li and C.T. Chan, "Double-negative acoustic metamaterial,"  
781 *Phys. Rev. E* **70**, 055602(R) (2004).

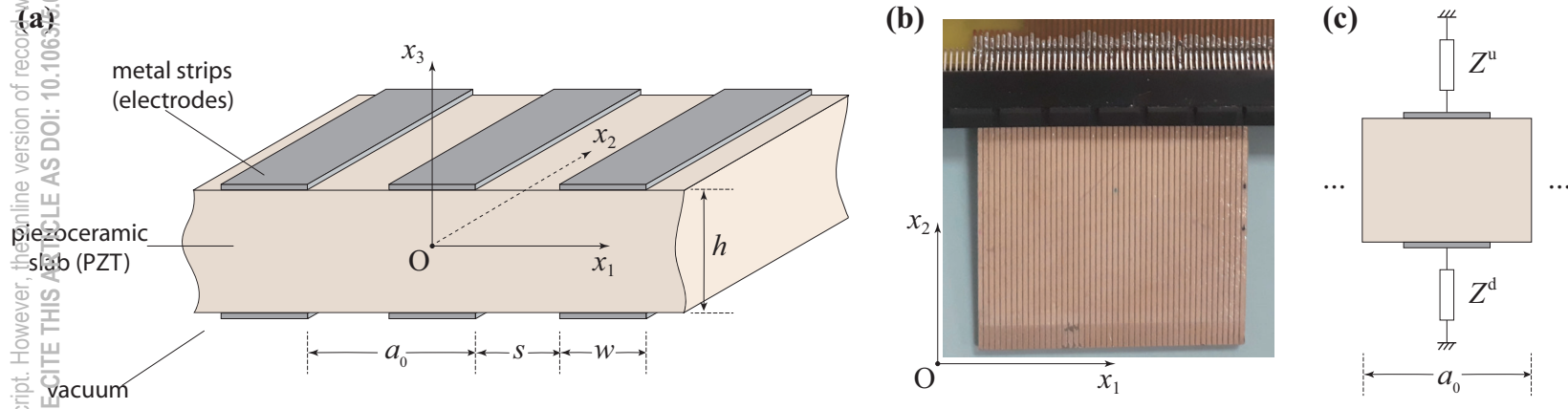
782 <sup>6</sup>A. Ba, A. Kovalenko, C. Aristégui, O. Mondain-Monval, and  
783 T. Brunet, "Soft porous silicone rubbers with ultra-low sound  
784 speeds in acoustic metamaterials," *Sci. Rep.* **7**, 40106 (2017).

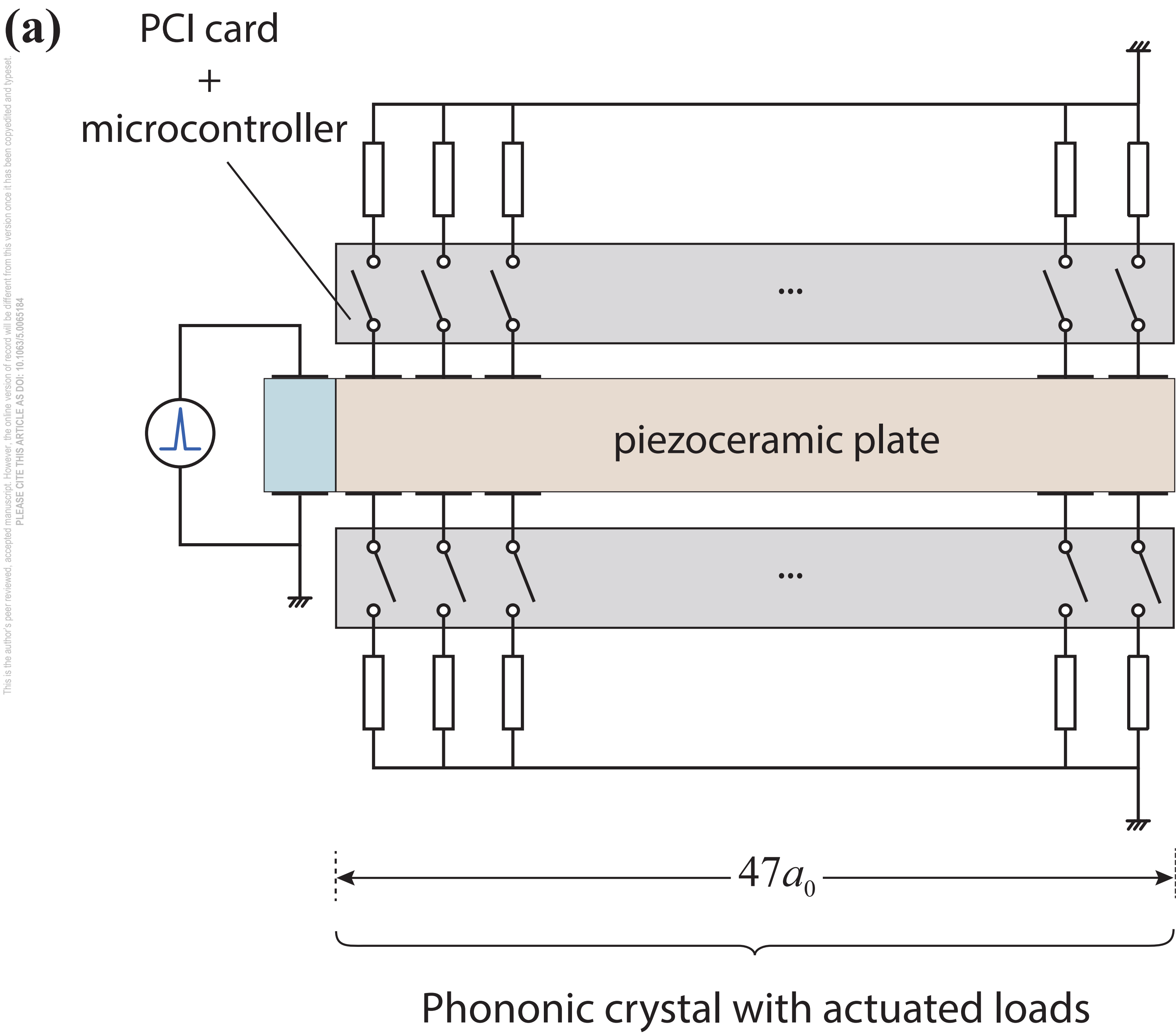
785 <sup>7</sup>P. Celli, B. Yousefzadeh, C. Daraio, and S. Gonella, "Bandgap  
786 widening by disorder in rainbow metamaterials," *Appl. Phys.*  
787 *Let.* **114**, 091903 (2019).

This is the author's peer reviewed, accepted manuscript. However, the online version of record will be different from this version once it has been copyedited and typeset.  
PLEASE CITE THIS ARTICLE AS DOI: 10.1063/5.0065184

- 788 <sup>8</sup>M. Miniaci, A. Krushynska, A.S. Gliozzi, N. Kherraz, F. Bosia, 830  
789 and N.M. Pugno, "Design and Fabrication of Bioinspired Hier- 831  
790 archical Dissipative Elastic Metamaterials," *Phys. Rev. Applied* 832  
791 **10**, 024012 (2018). 833
- 792 <sup>9</sup>Q.J. Lim, P. Wang, S.J.A. Koh, E.H. Khoo, and K. Bertoldi, 834  
793 "Wave propagation in fractal-inspired self-similar beam lattices," 835  
794 *Appl. Phys. Lett.* **107**, 221911 (2015). 836
- 795 <sup>10</sup>J.-F. Robillard, O. Bou Matar, J.O. Vasseur, P.A. Deymier, 837  
796 M. Stippinger, A.-C. Hladky-Hennion, Y. Pennec, and B. Djafari- 838  
797 Rouhani, "Tunable magnetoelastic phononic crystals," *Appl.* 839  
798 *Phys. Lett.* **95**, 124104 (2009). 840
- 799 <sup>11</sup>W. Qian, Z. Yu, X. Wang, Y. Lai, and B.B. Yellen, "Elastic 841  
800 metamaterial beam with remotely tunable stiffness," *J. Appl.* 842  
801 *Phys.* **119**, 055102 (2016). 843
- 802 <sup>12</sup>S.W. Xiao, G.C. Ma, Y. Li, Z.Y. Yang, and P. Sheng, "Ac- 844  
803 tive control of membrane-type acoustic metamaterial by electric 845  
804 field," *Appl. Phys. Lett.* **106**, 91904 (2015). 846
- 805 <sup>13</sup>Y. Cheng, X.J. Liu, and D.J. Wu, "Temperature effects on the 847  
806 band gaps of lamb waves in a one-dimensional phononic-crystal 848  
807 plate," *J. Acoust. Soc. Am.* **129**, 1157-1160 (2011). 849
- 808 <sup>14</sup>Z. Li, Y. Li, S. Kumar, and H.P. Lee, "Thermal tuning of negative 850  
809 effective mass density in a two-dimensional acoustic metamaterial 851  
810 with hexagonal lattice," *J. Appl. Phys.* **126**, 155102 (2019). 852
- 811 <sup>15</sup>E. Walker, D. Reyes, M.M. Rojas, A. Krokhin, Z. Wang, and 853  
812 A. Neogi, "Tunable ultrasonic phononic crystal controlled by in- 854  
813 frared radiation," *Appl. Phys. Lett.* **105**, 143503 (2014). 855
- 814 <sup>16</sup>A.S. Gliozzi, M. Miniaci, A. Chiappone, A. Bergamini, B. Morin, 856  
815 E. Descrovi, "Tunable photo-responsive elastic metamaterials," 857  
816 *Nat. Comm.* **11**, 2576 (2020). 858
- 817 <sup>17</sup>L. Airolidi and M. Ruzzene, "Design of tunable acoustic metama- 859  
818 terials through periodic arrays of resonant shunted piezos," *New* 860  
819 *J. Phys.* **13**, 113010 (2011). 861
- 820 <sup>18</sup>R. Zhu, Y.Y. Chen, M.V. Barnhart, G.K. Hu, C.T. Sun, and 862  
821 G.L. Huang, "Experimental study of an adaptive elastic metama- 863  
822 terial controlled by electric circuits," *Appl. Phys. Lett.* **108**, 864  
823 011905 (2016). 865
- 824 <sup>19</sup>C. Sugino, M. Ruzzene, and A. Erturk, "Design and analysis 866  
825 of piezoelectric metamaterial beams with synthetic impedance 867  
826 shunt circuits," *IEEE/ASME Trans. Mechatronics* **23**, 2144-55 868  
827 (2018). 869
- 828 <sup>20</sup>S. Degraeve, C. Granger, B. Dubus, J.O. Vasseur, M. Pham Thi, 870  
829 and A.-C. Hladky-Hennion, "Bragg band gaps tunability in an 871  
homogeneous piezoelectric rod with periodic electrical boundary 872  
conditions," *J. Appl. Phys.* **115**, 194508 (2014). 873
- <sup>21</sup>S. Degraeve, C. Granger, B. Dubus, J.O. Vasseur, M. Pham Thi, 874  
and A.-C. Hladky-Hennion, "Tunability of Bragg band gaps in 875  
one-dimensional piezoelectric phononic crystals using external 876  
capacitances," *Smart Mater. Struct.* **24**, 085013 (2015). 877
- <sup>22</sup>S.A. Mansoura, P. Benard, B. Morvan, P. Marechal, A.- 878  
C. Hladky-Hennion, and B. Dubus, "Theoretical and experimen- 879  
tal analysis of a piezoelectric plate connected to a negative ca- 880  
pacitance at MHz frequencies," *Smart Mater. Struct.* **24**, 115032 881  
(2015). 882
- <sup>23</sup>N. Kherraz, L. Haumesser, F. Levassort, P. Benard, and B. Mor- 883  
van, "Controlling Bragg gaps induced by electric boundary con- 884  
ditions in phononic piezoelectric plates," *Appl. Phys. Lett.* **108**, 885  
093503 (2016). 886
- <sup>24</sup>N. Kherraz, L. Haumesser, F. Levassort, P. Benard, and B. Mor- 887  
van, "Hybridization bandgap induced by an electrical resonance 888  
in piezoelectric metamaterial plates," *J. Appl. Phys.* **123**, 094901 889  
(2018). 890
- <sup>25</sup>N. Kherraz, F.H. Chikh-Bled, R. Sainidou, B. Morvan, and 891  
P. Rembert, "Tunable phononic structures using Lamb waves 892  
in a piezoceramic plate," *Phys. Rev. B* **99**, 094302 (2019). 893
- <sup>26</sup>F.H. Chikh-Bled, N. Kherraz, R. Sainidou, P. Rembert, and 894  
B. Morvan, "Piezoelectric phononic plates: retrieving the fre- 895  
quency band structure via all-electric experiments," *Smart* 896  
*Mater. Struct.* **28**, 115046 (2019). 897
- <sup>27</sup>We used the COMSOL Multiphysics v. 5.5 software to per- 898  
form the calculations ([www.comsol.com](http://www.comsol.com). COMSOL AB, Stock- 899  
holm, Sweden). 900
- <sup>28</sup><https://www.americanpiezo.com/>. 901
- <sup>29</sup>M. Tummala, "New algorithm for solving block matrix equations 902  
with applications in 2-D AR spectral estimation," *IEEE Trans.* 903  
*Signal Processing* **39**, 759-764 (1991). 904
- <sup>30</sup>N. W. Ashcroft and N. D. Mermin, *Solid State Physics* (New 905  
York: Saunders College Publishing, 1976). 906
- <sup>31</sup>The equivalent electric circuit that models this unit cell coincides 907  
to that shown in Fig.A1(b) of Ref. 26, and the dispersion relation 908  
of this mode is still given by Eq.(2) of the above-mentioned 909  
reference. 910
- <sup>32</sup>R. Sainidou, N. Stefanou, I.E. Psarobas, and A. Modinos, "Scat- 911  
tering of elastic waves by a periodic monolayer of spheres," *Phys.* 912  
*Rev. B* **66**, 024303 (2002). 913

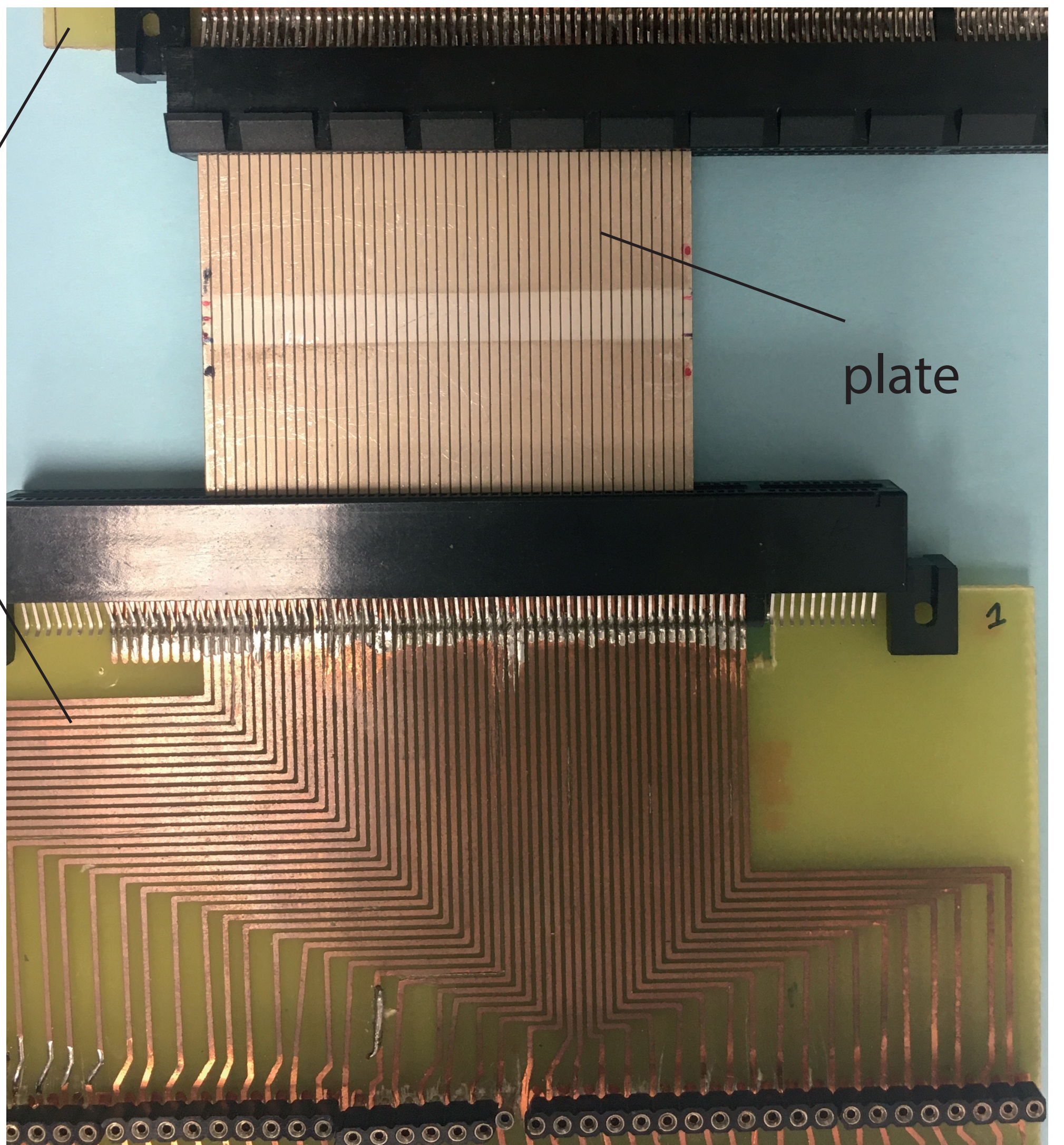
This is the author's peer reviewed, accepted manuscript. However, the online version of records will be different from this version once it has been copyedited and typeset.  
PLEASE CITE THIS ARTICLE AS DOI: 10.1063/1.50065184



**(b)**

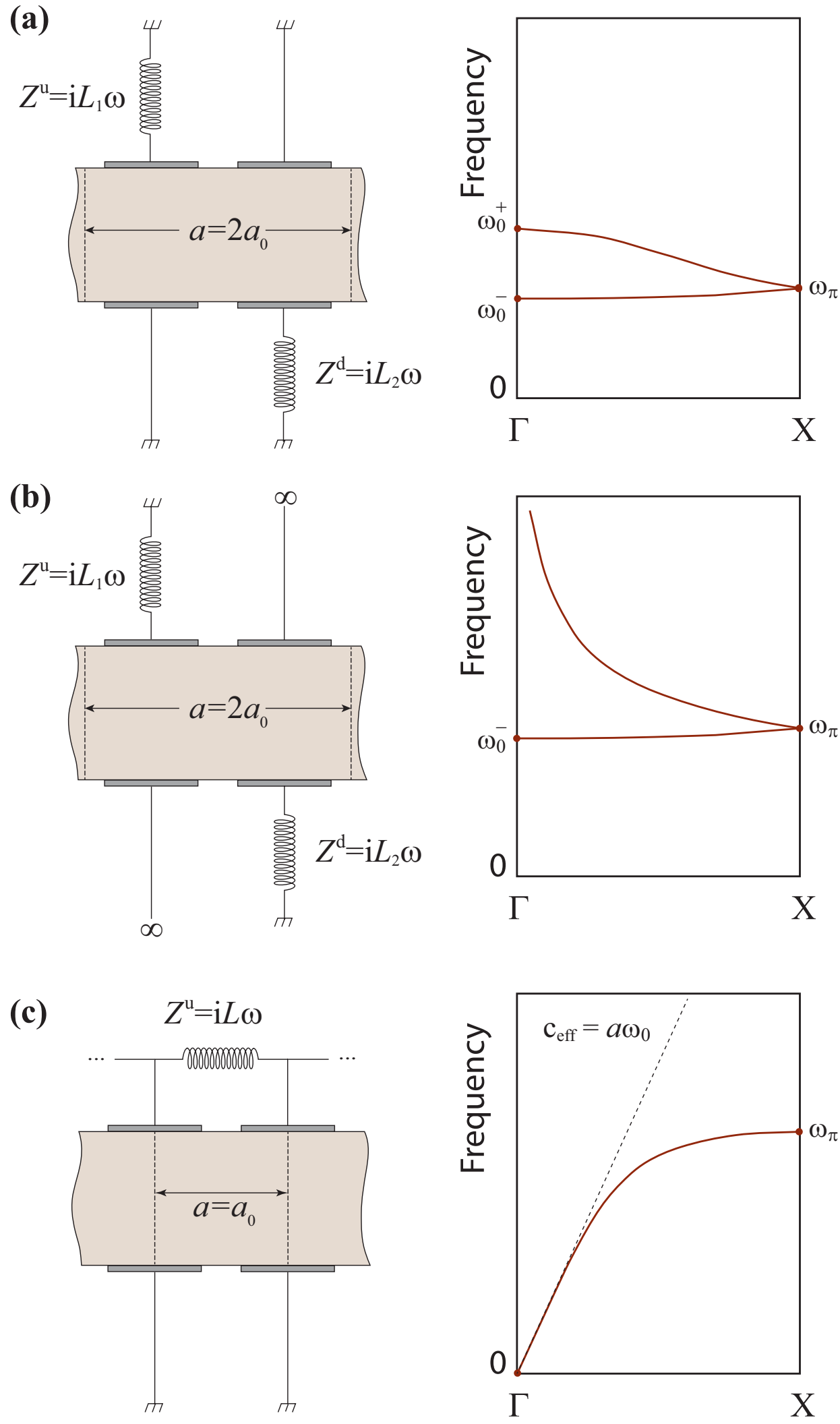
PCI cards

plate

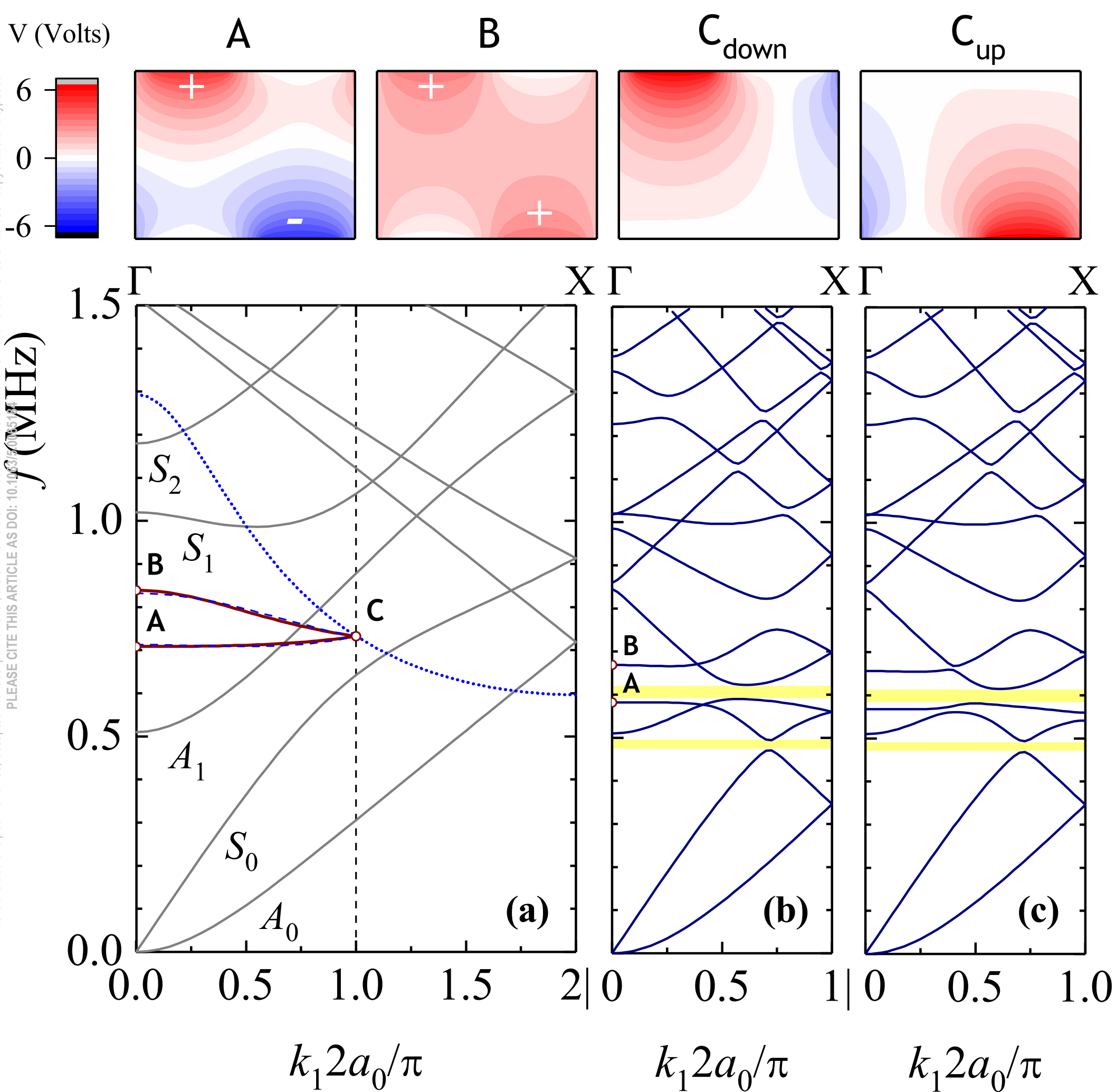




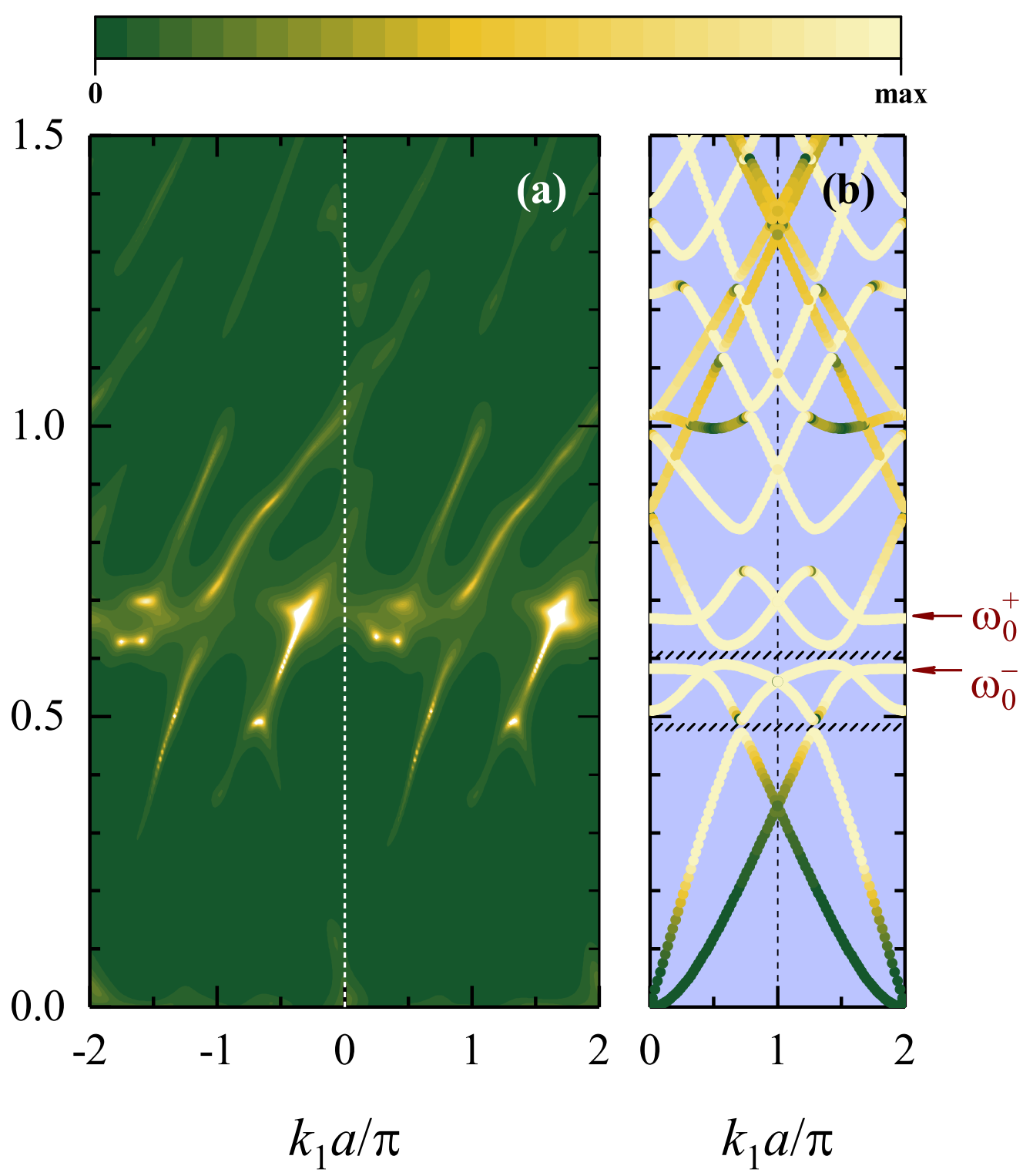
This is the author's peer reviewed, accepted manuscript. However, the online version of record will be different from this version once it has been copyedited and typeset.  
PLEASE CITE THIS ARTICLE AS DOI: 10.1063/5.0065184



This is the author's peer reviewed, accepted manuscript. However, the online version of record will be different from this version once it has been copyedited and typeset. PLEASE CITE THIS ARTICLE AS DOI: 10.1063/1.5003514

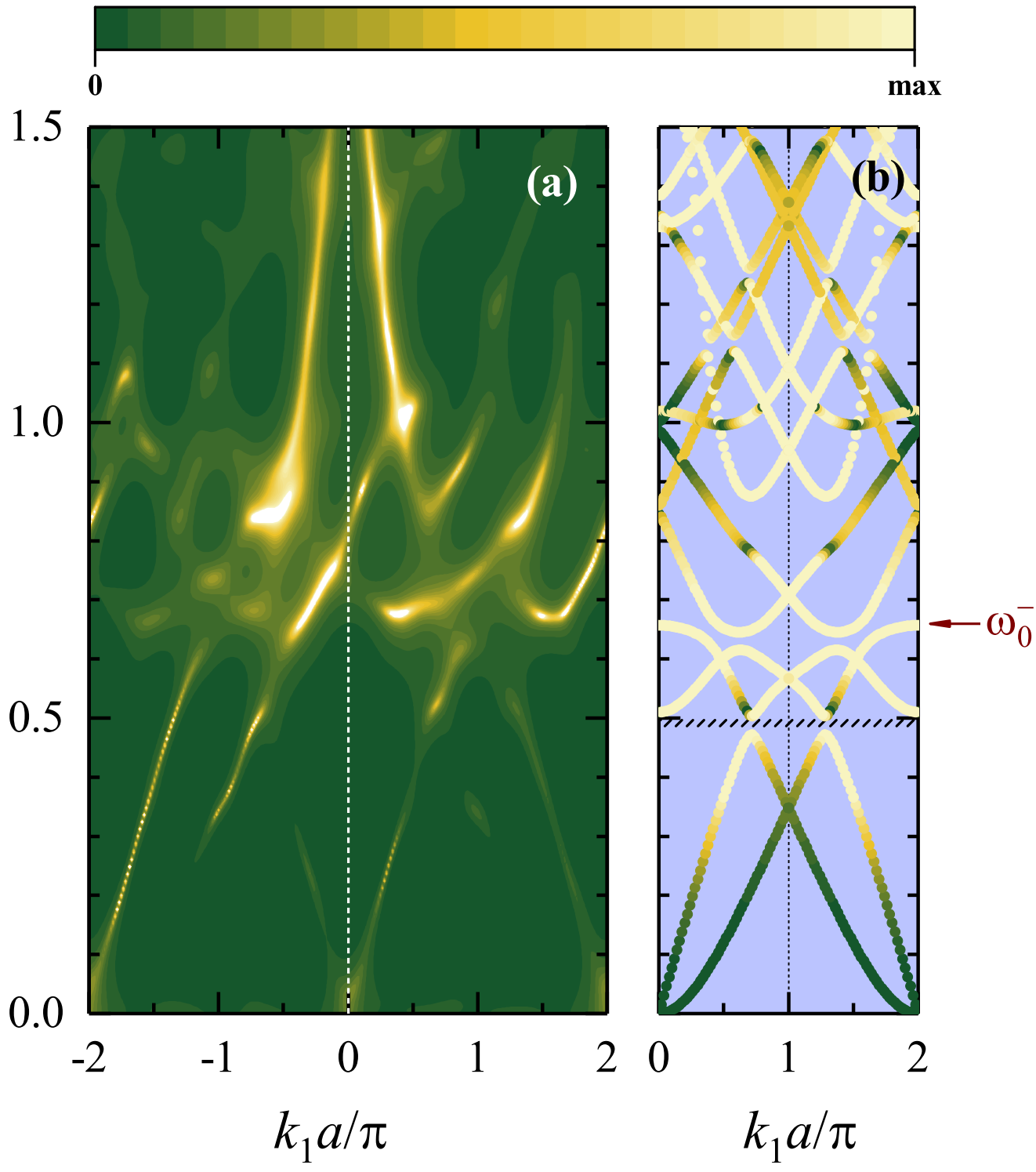


This is the author's peer reviewed, accepted manuscript. However, the online version of record will be different from this version once it has been copyedited and typeset.  
PLEASE CITE THIS ARTICLE AS DOI: 10.1063/5.0065184

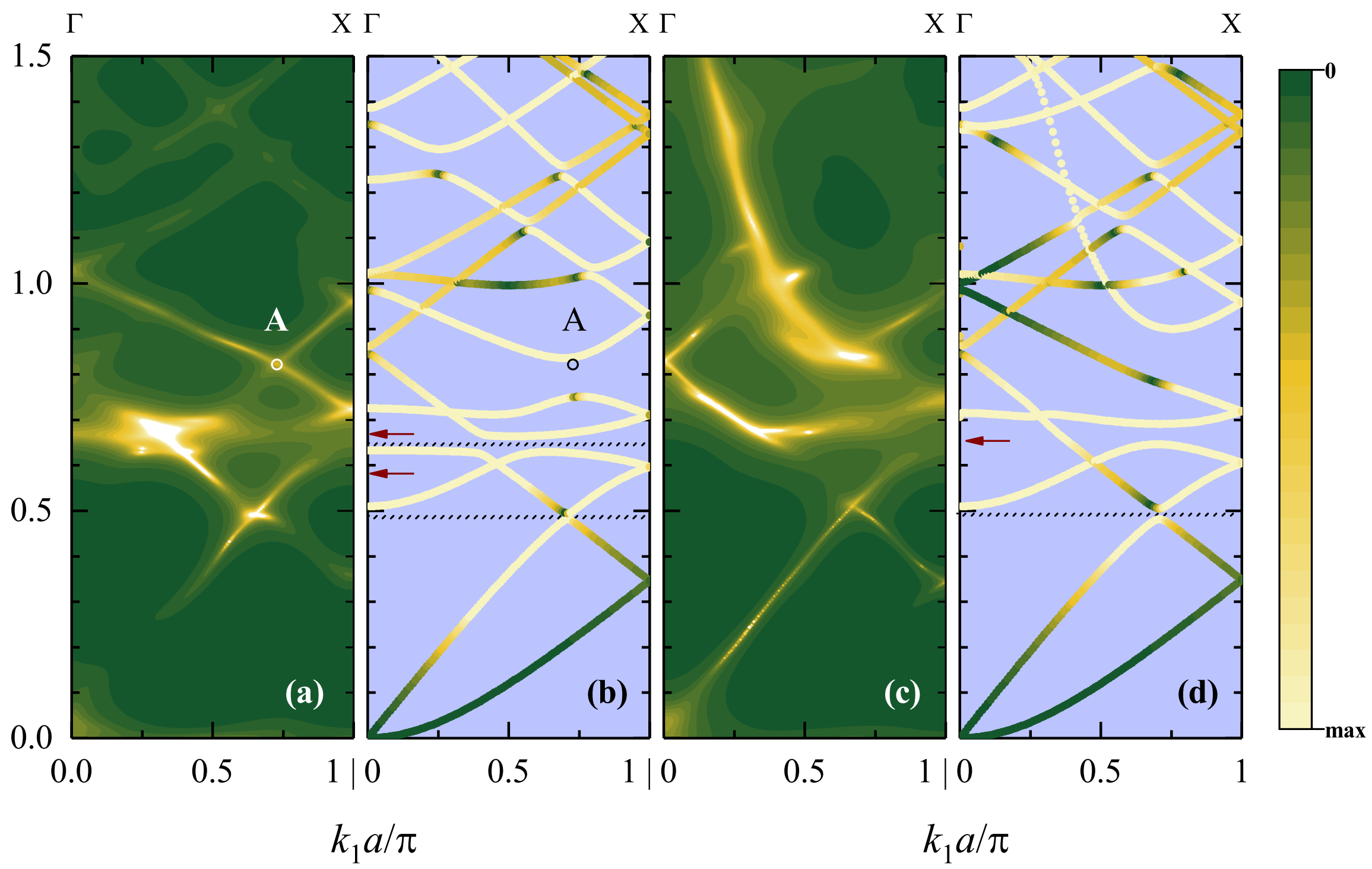


This is the author's peer reviewed, accepted manuscript. However, the online version of record will be different from this version once it has been copyedited and typeset.  
PLEASE CITE THIS ARTICLE AS DOI: 10.1063/5.0065184

$f$  (MHz)



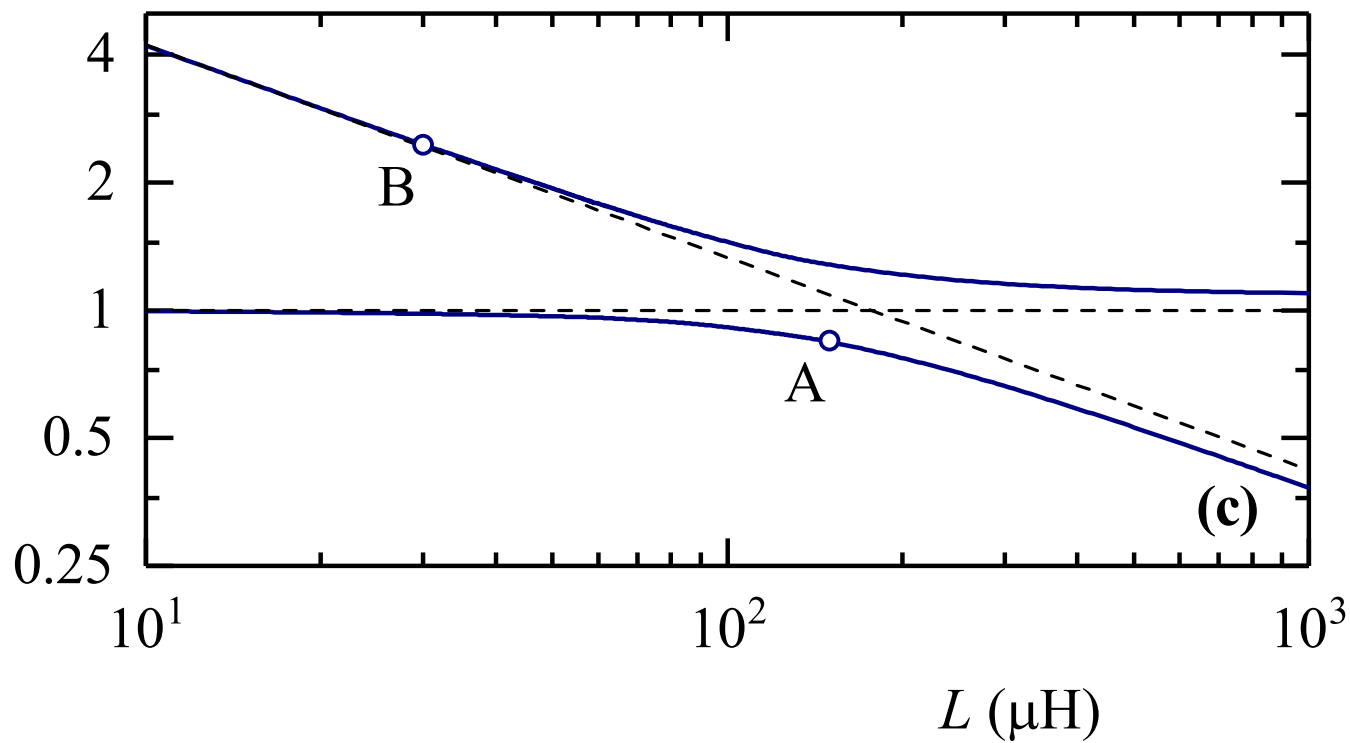
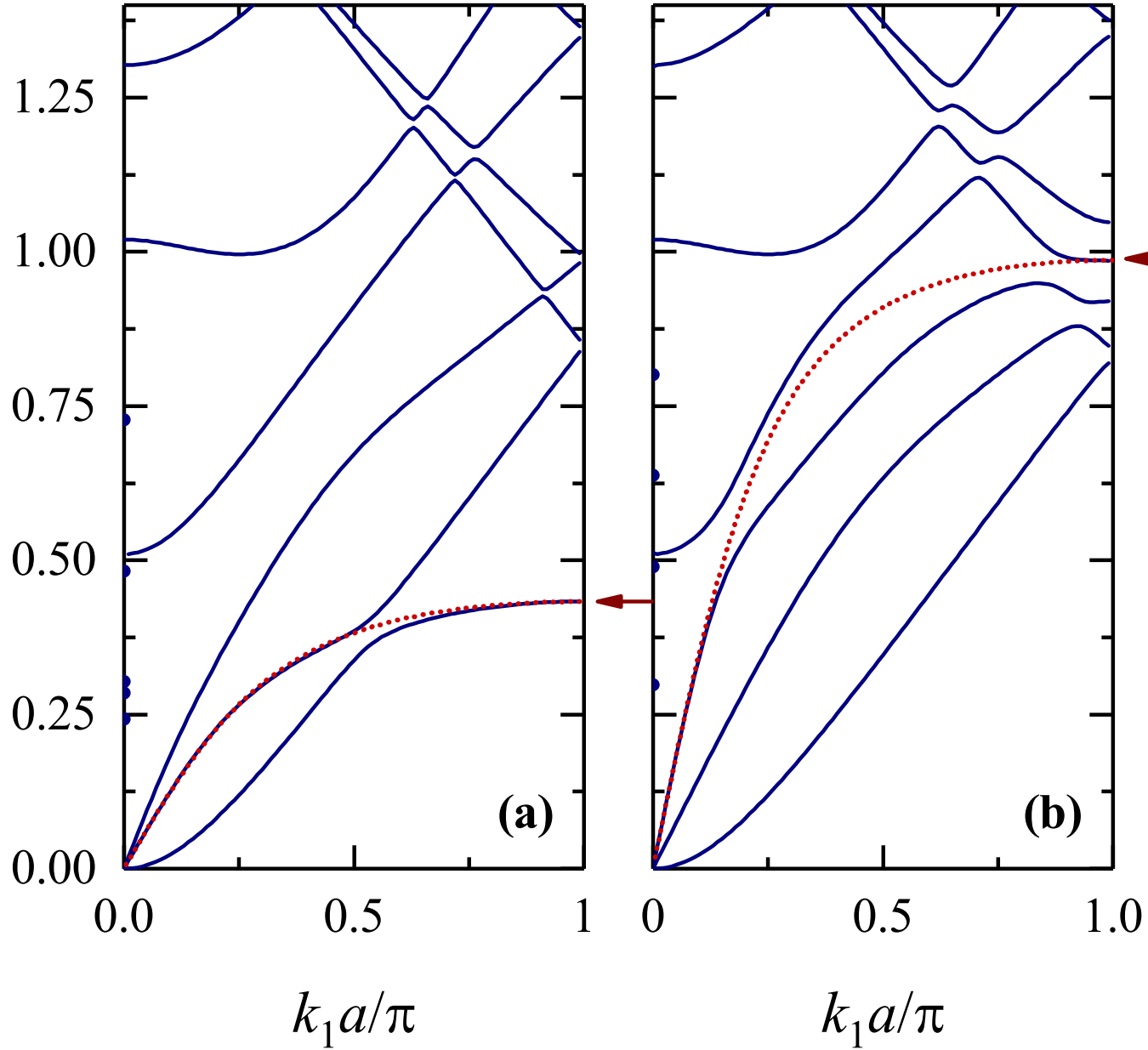
This is the author's peer reviewed, accepted manuscript. However, the online version of record will be different from this version once it has been copyedited and typeset.  
PLEASE CITE THIS ARTICLE AS DOI: 10.1063/5.0065184



This is the author's peer reviewed, accepted manuscript. However, the online version of record will be different from this version once it has been copyedited and typeset.

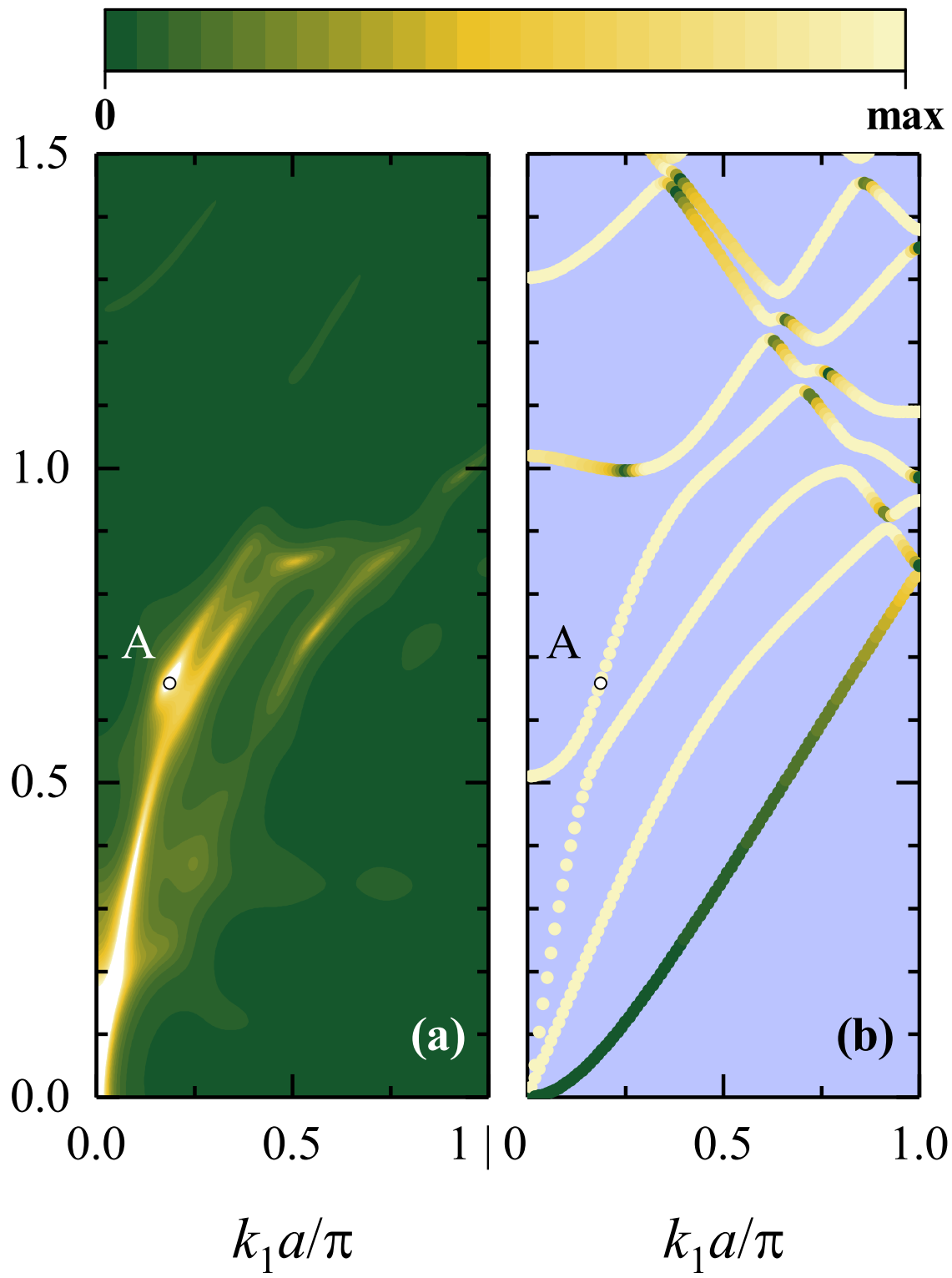
PLEASE CITE THIS ARTICLE AS DOI: 10.1063/5.0065184

$f$  (MHz)

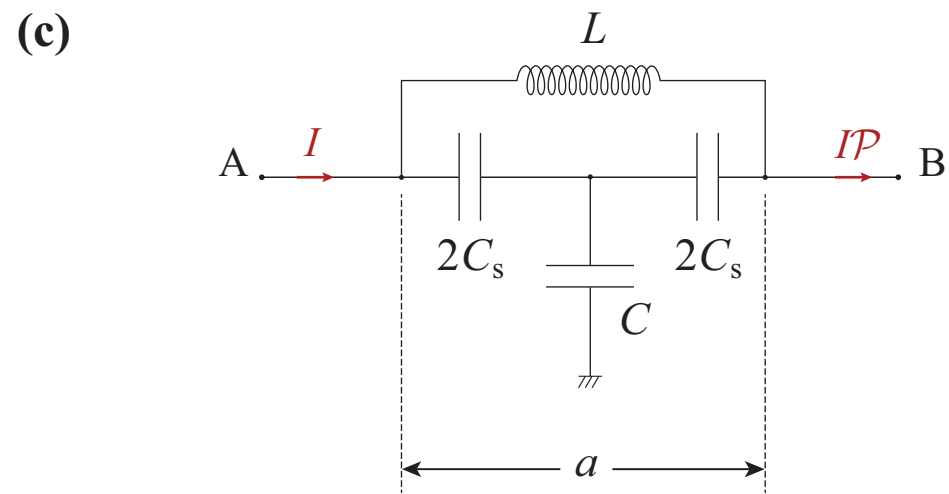
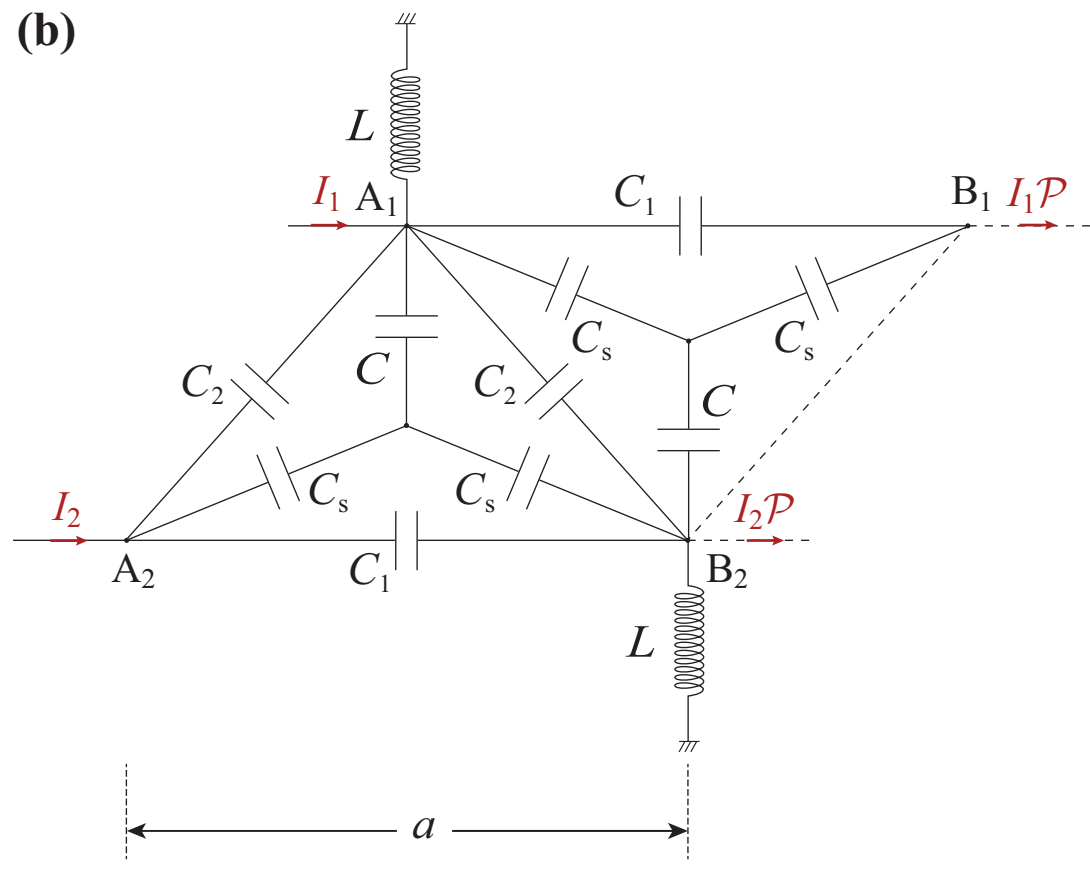
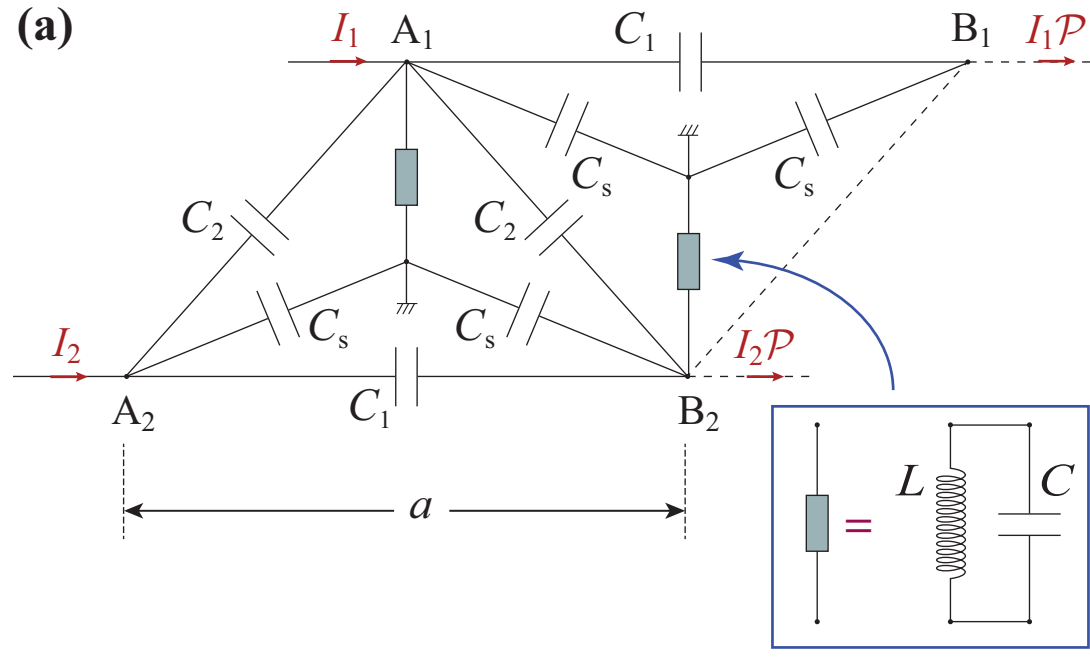


This is the author's peer reviewed, accepted manuscript. However, the online version of record will be different from this version once it has been copyedited and typeset.  
PLEASE CITE THIS ARTICLE AS DOI: 10.1063/5.0065184

$f$  (MHz)

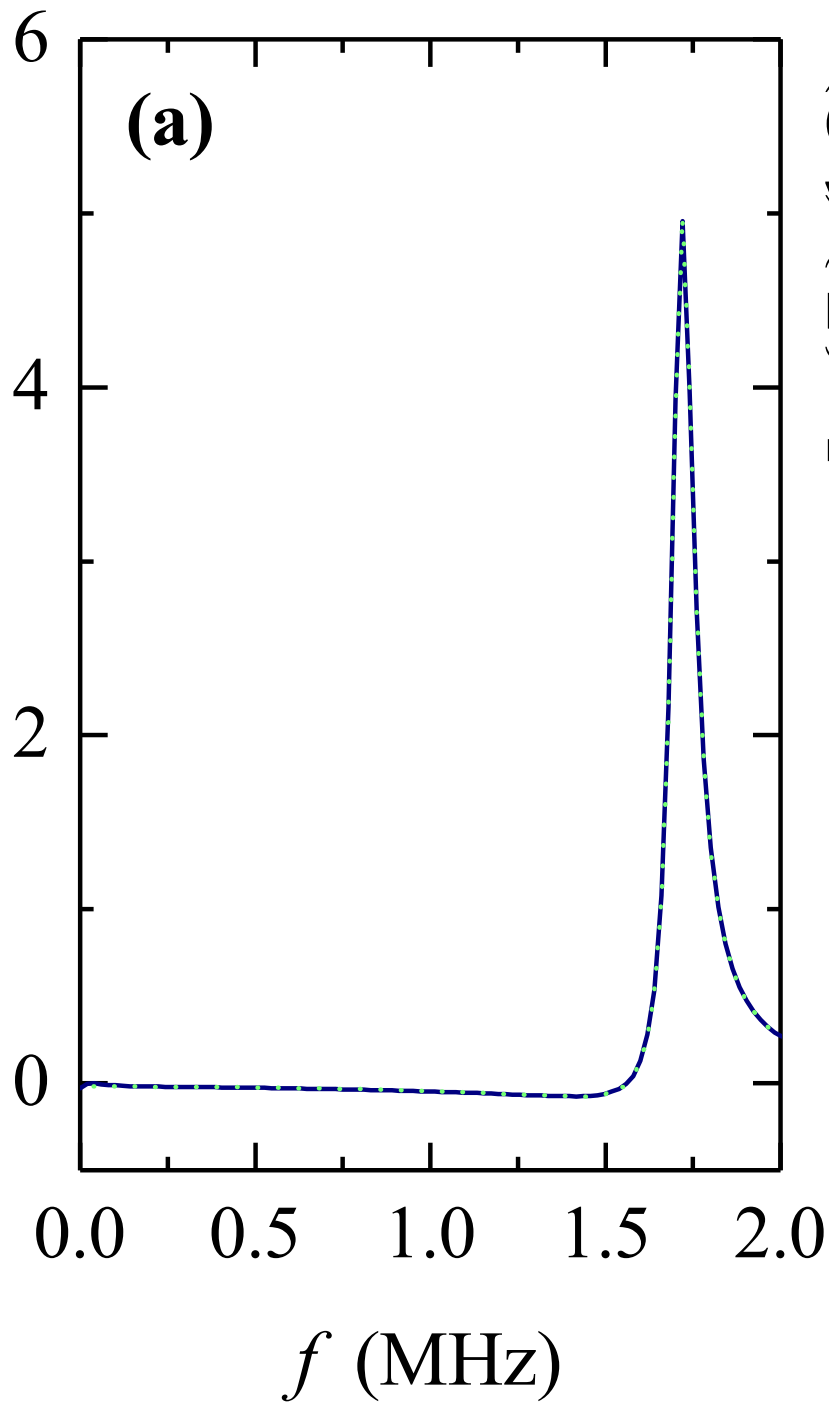


This is the author's peer reviewed, accepted manuscript. However, the online version of record will be different from this version once it has been copyedited and typeset.  
 PLEASE CITE THIS ARTICLE AS DOI: 10.1063/5.0065184





This is the author's peer reviewed, accepted manuscript. However, the online version of record will be different from this version once it has been copyedited and typeset.  
PLEASE CITE THIS ARTICLE AS DOI: 10.1063/5.0065184

 $\text{Re}\{Z_e\}$  (k $\Omega$ ) $\text{Im}\{Z_e\}$  (k $\Omega$ )